The Interstellar Medium in I Zw 18 Seen with JWST/MIRI. I. Highly Ionized Gas

Hunt, L. K.; Aloisi, A.; Navarro, M. G.; Rickards Vaught, R. J.; Draine, B. T.; Adamo, A.; Annibali, F.; Calzetti, D.; Brandl, B.; More Authors

DOI
10.3847/1538-4357/adfb69

Publication date
2025

Document Version
Final published version

Published in
Astrophysical Journal

The Astrophysical Journal, 992:48 (22pp), 2025 October 10 https://doi.org/10.3847/1538-4357/adfb69

The Interstellar Medium in I Zw 18 Seen with JWST/MIRI. I. Highly Ionized Gas

L. K. Hunt[1], A. Aloisi[2,22], M. G. Navarro[3], R. J. Rickards Vaught[2], B. T. Draine[4], A. Adamo[5], F. Annibali[6], D. Calzetti[7], S. Hernandez[8], B. L. James[8], M. Mingozzi[2,8], R. Schneider[9,10,11,12], M. Tosi[6], B. Brandl[13,14], M. G. del Valle-Espinosa[2], F. Donnan[15], A. S. Hirschauer[16], M. Meixner[17], D. Rigopoulou[18,19], C. T. Richardson[20], J. M. Levanti[20], and A. R. Basu-Zych[21]

[1] INAF—Osservatorio Astrofisico di Arcetri, Largo E. Fermi 5, 50125 Firenze, Italy; leslie.hunt@inaf.it
[2] Space Telescope Science Institute, 3700 San Martin Drive, Baltimore, MD 21218, USA
[3] INAF—Osservatorio Astronomico di Roma, Via di Frascati 33, 00040 Monteporzio Catone, Italy
[4] Department of Astrophysical Sciences, Princeton University, Princeton, NJ 08544, USA
[5] Department of Astronomy, The Oskar Klein Centre, Stockholm University, AlbaNova, SE-10691 Stockholm, Sweden
[6] INAF—Osservatorio di Astrofisica e Scienza dello Spazio, Via Gobetti 93/3, 40129 Bologna, Italy
[7] Department of Astronomy, University of Massachusetts Amherst, 710 North Pleasant Street, Amherst, MA 01003, USA
[8] AURA for ESA, Space Telescope Science Institute, 3700 San Martin Drive, Baltimore, MD 21218, USA
[9] Dipartimento di Fisica, "Sapienza" Università di Roma, Piazzale Aldo Moro 2, I-00185 Roma, Italy
[10] INAF—Osservatorio Astronomico di Roma, Via di Frascati 33, I-00040 Monte Porzio Catone, Italy
[11] INFN, Sezione Roma1, Dipartimento di Fisica, "Sapienza" Università di Roma, Piazzale Aldo Moro 2, I-00185 Roma, Italy
[12] Sapienza School for Advanced Studies, Viale Regina Elena 291, I-00161 Roma, Italy
[13] Leiden Observatory, Leiden University, P.O. Box 9513, 2300 RA Leiden, The Netherlands
[14] Faculty of Aerospace Engineering, Delft University of Technology, Kluyverweg 1, 2629 HS Delft, The Netherlands
[15] Department of Physics, University of Oxford, Keble Road, Oxford, OX1 3RH, UK
[16] Department of Physics & Engineering Physics, Morgan State University, 1700 East Cold Spring Lane, Baltimore, MD 21251, USA
[17] Jet Propulsion Laboratory, California Institute of Technology, 4800 Oak Grove Drive, Pasadena, CA 91109, USA
[18] Department of Physics, University of Oxford, Keble Road, Oxford OX1 3RH, UK
[19] School of Sciences, European University Cyprus, Diogenes Street, Engomi, 1516 Nicosia, Cyprus
[20] Department of Physics & Astronomy, Elon University, 100 Campus Drive, Elon, NC 27244, USA
[21] NASA Goddard Flight Center, Code 662, Greenbelt, MD 20771, USA
[22] Astrophysics Division, Science Mission Directorate, NASA Headquarters, 300 E Street SW, Washington, DC 20546, USA
Received 2025 April 18; revised 2025 August 5; accepted 2025 August 11; published 2025 October 6

Abstract

We present JWST/MIRI spectra from the Medium-Resolution Spectrometer of I Zw 18, a nearby dwarf galaxy with a metallicity of ∼3% solar. Its proximity enables a detailed study of highly ionized gas that can be interpreted in the context of newly discovered high-redshift dwarf galaxies. We derive aperture spectra centered on 11 regions of interest; the spectra show very low extinction, $A_V \lesssim 0.1$, consistent with optical determinations. The gas is highly ionized; we have detected 10 fine-structure lines, including [O IV] 25.9 μm with an ionization potential (IP) of ∼55 eV, and [Ne V] 14.3 μm with an IP of ∼97 eV. The ionization state of I Zw 18 falls at the extreme upper end of all of the line ratios we analyzed, but not coincident with galaxies containing an accreting massive black hole (active galactic nucleus). Comparison of the line ratios with state-of-the-art photoionization and shock models suggests that the high-ionization state in I Zw 18 is not due to shocks. Rather, it can be attributed to metal-poor stellar populations with a self-consistent contribution of X-ray binaries or ultra-luminous X-ray sources. It could also be partially due to a small number of hot low-metallicity Wolf−Rayet stars ionizing the gas; a small fraction (a few percent) of the ionization could come from an intermediate-mass black hole. Our spectroscopy also revealed four 14 μm continuum sources, ≳30–100 pc in diameter, three of which were not previously identified. Their properties are consistent with H II regions ionized by young star clusters.

Unified Astronomy Thesaurus concepts: Compact dwarf galaxies (281); Dwarf irregular galaxies (417); Interstellar medium (847); Young star clusters (1833)

1. Introduction

Dwarf galaxies (stellar mass $M_* \lesssim 10^9\,M_\odot$) are the smallest, faintest, least chemically evolved systems in the Universe, and the most abundant galaxy population at any redshift (e.g., S. D. M. White & C. S. Frenk 1991; A. Babul & H. C. Ferguson 1996; J. S. Bullock & M. Boylan-Kolchin 2017; I. Davidzon et al. 2017; M. Stefanon et al. 2021). In the Λ cold dark matter paradigm, dwarf galaxies resided in early low-mass dark matter (DM) haloes ($\lesssim 10^{11}\,M_\odot$; J. S. Bullock & M. Boylan-Kolchin 2017; P. Behroozi et al. 2019, 2020) that were the sites of the first star formation (SF). Due to their high ionizing photon escape fractions, the dwarf galaxies forming in low-mass DM halos are thought to provide most of the photons needed to reionize the Universe (e.g., J. H. Wise & R. Cen 2009; H. Atek et al. 2022, 2024). They are also expected to be extremely metal-poor, with a rapid transition from virtually pristine (Population III) stars in mini-haloes to the few percent level of metal enrichment relative to solar metallicity ($Z_\odot$) that can be observed today (e.g., V. Bromm & N. Yoshida 2011; R. S. Klessen & S. C. O. Glover 2023).

Before the advent of JWST, it was virtually impossible to study dwarf galaxies in detail at or beyond the Epoch of Reionization. Now, early observations have revealed a wealth

of information about metal-poor dwarf galaxies at those redshifts (L. J. Furtak et al. 2023; K. E. Heintz et al. 2023; J. E. Rhoads et al. 2023; J. R. Trump et al. 2023; M. Curti et al. 2024; T. Morishita et al. 2024). These new observations find that the majority of galaxies at $z \gtrsim 7$ are dwarfs ($M_* \lesssim 10^8\,M_\odot$; A. C. Carnall et al. 2023; L. J. Furtak et al. 2023; K. Nakajima et al. 2023; R. Endsley et al. 2024), with low metallicities ($Z/Z_\odot \lesssim 0.2$; A. C. Carnall et al. 2023; M. Curti et al. 2023, 2024; J. R. Trump et al. 2023; J. E. Rhoads et al. 2023; T. Morishita et al. 2024). These high-z dwarf galaxies also exhibit high star formation rates (SFRs) for their stellar mass, a consequence of the evolutionary shift of SFR/M_* to higher values at higher redshifts (e.g., K. G. Noeske et al. 2007; J. S. Speagle et al. 2014; K. E. Whitaker et al. 2014; S. K. Leslie et al. 2020; C. J. Conselice et al. 2025), and the tendency of low-mass galaxies at high redshift to have "'bursty" Star Formation (SF) histories, unlike their more-massive counterparts (T. J. Looser et al. 2025). Although these preliminary JWST results are not definitive, they hint at extremely intense SF activity in these dwarf galaxies at very early epochs.

Despite their cosmological importance, it is not yet clear how metal-poor dwarfs fit within the current framework for massive SF. The interstellar medium (ISM) in these systems tends to be less dusty (e.g., A. Rémy-Ruyer et al. 2014; F. Galliano et al. 2021), therefore with less shielding from the intense radiation field (RF) produced by massive stars. Cooling is inefficient because of the low metal and dust content. Overall, this results in a paucity of ISM diagnostics such as CO, the usual proxy for H_2, because it tends to be photodissociated in unshielded metal-poor environments (e.g., E. F. van Dishoeck & J. H. Black 1988; A. D. Bolatto et al. 2013). At low metallicity, there is also a deficit of dust features such as those emitted by polycyclic aromatic hydrocarbons (PAHs; e.g., C. W. Engelbracht et al. 2005; S. C. Madden et al. 2006; L. K. Hunt et al. 2010). The RF tends to be harder and more intense at low metallicity (e.g., D. Cormier et al. 2015), and able to effectively carve cavities in the surrounding neutral ISM. This makes the ISM more porous and clumpy than in less extreme environments. However, the resolved chemical and ionization structure of the ISM is virtually impossible to study in dwarf galaxies at high redshift, requiring us to study examples in the Local Universe.

Objects like the recently discovered JWST high-z dwarf galaxies do exist in the Local Universe, namely blue compact dwarf galaxies (BCDs), defined by high surface brightness and blue optical colors (e.g., A. Gil de Paz et al. 2003). At a distance of 18.2 Mpc (88 pc arcsec^{-1}; A. Aloisi et al. 2007), the most extreme BCD is I Zw 18, with a metallicity of 12+log (O/H) = 7.2 ($\sim$3% $Z_\odot$; Y. I. Izotov et al. 1999; V. Lebouteiller et al. 2013),[23] among the lowest in the nearby Universe, a stellar mass of $\sim 10^6$–$10^7\,M_\odot$ (M. Fumagalli et al. 2010; S. C. Madden et al. 2014; S. Janowiecki et al. 2017; A. Nanni et al. 2020), and an SFR estimated from the radio free–free continuum of $\sim 0.2\,M_\odot\,\mathrm{yr}^{-1}$ (L. K. Hunt et al. 2005). Over the last 10 Myr, the SFR is estimated to have been greater, $\lesssim 1\,M_\odot\,\mathrm{yr}^{-1}$ (F. Annibali et al. 2013; G. Bortolini et al. 2024). Its specific SFR (sSFR = SFR/M_*) is very high, $\sim 10^{-7}$–$10^{-8}\,\mathrm{yr}^{-1}$, making I Zw 18 a "starburst", lying well above the local SF main sequence. It is thus an ideal target to characterize with high spatial definition the ISM and the massive SF taking place in an almost pristine environment similar to that of the dwarf galaxies newly discovered at redshift $z \gtrsim 7$ by JWST.

I Zw 18 is extremely gas rich with $\sim 1 \times 10^8\,M_\odot$ of H I (L. van Zee et al. 1998; F. Lelli et al. 2012); its main body is interacting with a fainter companion (I Zw 18 C, or "Zwicky's flare") $\sim$1.5 kpc to the NW, embedded in the same H I envelope (L. van Zee et al. 1998). The radio continuum at 5 GHz in I Zw 18 is optically thin (J. M. Cannon et al. 2005; L. K. Hunt et al. 2005) indicating lack of self-absorption from dense (ionized) gas. The lack of dense gas is also implied by the measured ionized-gas density of $\sim$ 10–100 cm^{-3}, both from optical spectra and inferred from the radio continuum (Y. I. Izotov et al. 1999; L. K. Hunt et al. 2005). SF in I Zw 18 is mostly concentrated in two prominent OB associations (NW, SE), each $\sim$ 200 pc in diameter, separated by $\sim$ 450 pc. Together they host a total of $\sim$2000 O stars (D. A. Hunter & H. A. Thronson 1995; J. M. Cannon et al. 2005; L. K. Hunt et al. 2005), similar to normal OB associations in the Milky Way.

In the optical, I Zw 18 emits high-ionization lines ([Fe V], He II) with ionization potentials required to create the corresponding ions of $\geqslant$54.4 eV, indicating an extremely hard RF (e.g., T. X. Thuan & Y. I. Izotov 2005). The He II emission cannot be explained with a "standard" massive stellar population, including Wolf–Rayet stars (C. Kehrig et al. 2015), and has been attributed to Population III stars (e.g., C. Kehrig et al. 2015, 2016), or possibly luminous X-ray binaries (XRBs; D. Schaerer et al. 2019; R. J. Rickards Vaught et al. 2021), because of the bright X-ray source associated with the NW OB complex (T. X. Thuan et al. 2004; P. Kaaret & H. Feng 2013). There are also hints of faint extended diffuse X-ray emission (T. X. Thuan et al. 2004), which could be associated with superbubbles driven by massive stellar feedback (e.g., C. L. Martin 1996).

There is apparently little cool dust in I Zw 18. Optical and near-infrared H recombination lines indicate very low extinction ($A_V \sim$ 0–0.2 mag; Y. I. Izotov et al. 1999; Y. I. Izotov & T. X. Thuan 2016), making I Zw 18 ostensibly similar to the pristine environments of primordial galaxies. The total dust mass in I Zw 18 constrained by fitting the spectral energy distribution (SED) over almost 6 orders of magnitude in wavelength from the UV to the radio amounts to $\sim 340\,M_\odot$ (L. K. Hunt et al. 2014); estimated with a different dust model, it could be as high as $\sim 1800\,M_\odot$ (D. B. Fisher et al. 2014). I Zw 18 has been observed with Spitzer/IRS (Y. Wu et al. 2007), but the coarse spatial resolution made it impossible to separate the individual OB complexes, and the spectral resolution was low. Nevertheless, Y. Wu et al. (2007) detected [O IV] 25.89, consistent with the hard RF suggested by the optical high-ionization lines.

Here we present JWST MIRI Medium Resolution Integral Field Unit Spectrometer (MRS) observations of I Zw 18 at a spatial resolution $\sim 25 - 50$ pc. Our JWST observations reveal high-ionization gas, several H I recombination lines, and a full complement of H_2 transitions, but no strong emission from PAHs. In the following, we first describe the observations, data processing, and analysis in Section 2. The ionized-gas lines detected in spectra extracted within several regions of interest are presented in Section 3, and compared with state-of-the-art photoionization and shock models of the observed line ratios. Newly identified compact continuum sources that may be

[23] The O/H determination is discussed in Rickards Vaught et al., Paper III in this series.

young stellar clusters (YSCs) are described in Section 4. We discuss our results in Section 5, and give our conclusions in Section 6. Subsequent papers will describe other aspects of the data including the detection of warm molecular hydrogen, dust features, and the search for PAH emission (L. K. Hunt et al. 2025, hereafter Paper II); metallicity maps with [O IV] (R. J. Rickards Vaught et al. 2025); emission-line maps (L. K. Hunt et al. 2025, in preparation); and RF hardness inferred from line-ratio maps (R. J. Rickards Vaught et al. 2025, in preparation).

2. MIRI/MRS Data, Analysis, and Ancillary Data

I Zw 18 was observed on 2024 March 8 with the JWST MIRI MRS (I. Argyriou et al. 2023) through the GO program No. 3353 (PI Aloisi/coPI Hunt). Two pointings were executed, each of ∼8 hr duration, in order to sufficiently cover both the NW and SE OB associations; a separate background observation of the same duration was also acquired in the context of an uninterruptible sequence. We required a PA orientation range during the dedicated background observations to be able to acquire on-source MIRI imaging in F560W (5.6 μm), F1130W (11.3 μm), and F2550W (25.5 μm) to complement the filters acquired by GTO program No. 1233 (PI Meixner, see A. S. Hirschauer et al. 2024; G. Bortolini et al. 2024). The MRS spectral cubes comprise all three gratings, SHORT, MEDIUM, and LONG, for spectral coverage from $\sim 5 - 28\,\mu$m with a spectral resolving power ranging from ~ 1550 to 3250. We adopted a 4-point dither pattern optimized for extended sources, and used the SLOWR1 readout pattern, with 40 groups per integration and 2 integrations per exposure.

The MIRI data were reduced using the JWST calibration pipeline version 1.15.1 (H. Bushouse et al. 2024), with the corresponding CRDS (Calibration Reference Data System) context `jwst_1276.pmap` and CRDS file version 11.17.25. The data were processed through all three steps of the pipeline, with additional corrections applied to intermediate products outside the pipeline. Details of the reduction procedures are given in Appendix A. The final cubes were combined using the `drizzle` method (D. R. Law et al. 2023), for each of the four channels, conserving the native wavelength coverage and pixel sizes (e.g., 0.″13, 0.″17, 0.″20, 0.″35, for Channels 1, 2, 3, and 4, respectively).

2.1. Ancillary Data

We include in our analysis images/cubes of I Zw 18 at optical wavelengths. The Hubble Space Telescope (HST)/Advanced Camera for Surveys (ACS) F606W image of I Zw 18 is taken from A. Aloisi et al. (2007), but here realigned to the Gaia DR3 (Gaia Collaboration et al. 2021) astrometric system.

We also rely on the optical data cube from the Keck Cosmic Web Imager (KCWI) provided by R. J. Rickards Vaught et al. (2021). The angular resolution in the KWCI cube was derived from standard-star observations and is characterized by a full-width half-maximum (FWHM) of 0.″7, with a pixel scale of $\sim 0.''15$. The spectral resolving power is $R = 3600$, with a wavelength coverage between 3700 and 5500 Å. For more details, see R. J. Rickards Vaught et al. (2021). After alignment with the astrometrically corrected HST F606W image, the KWCI cube was convolved to the 27 μm MIRI point-spread function (PSF) using the same procedure described below in Section 2.2. Optical spectra within the apertures described below have been extracted from this convolved cube. In particular, Hβ and Hδ from KCWI will be used for the optical extinction estimate, and Hβ for line ratios relative to the MIRI H I recombination lines.

2.2. Aperture Spectra

In order to ensure that the line ratios within each aperture are mutually consistent, it was necessary to convolve the original data cubes to the PSF of the longest wavelength of interest ($\sim$27 μm). We first assumed that the MIRI PSF is described by a Gaussian; then the MIRI PSF FWHM at each wavelength was estimated according to D. R. Law et al. (2023; see their Equation (1)). The final Gaussian kernel σ_λ was calculated as $\mathrm{FWHM}_\lambda = \sqrt{8\ln 2}\,\sigma_\lambda$. The kernel width is defined as the quadrature difference for each λ plane in the cube, with a width $\sigma = \sqrt{\sigma_{27}^2 - \sigma_\lambda^2}$, where σ_λ is the intrinsic PSF σ at a given wavelength. These kernels were then convolved with the original cube to achieve 27 μm spatial resolution over each of the wavelength planes in the cube.

Spectra were extracted from the convolved cubes from apertures with a radius of 0.″65 ($\sim$120 pc diameter), centered on 11 regions of interest. These regions of interest include the four H II regions, dubbed VLA-NW-A, -B, -C, and VLA-SE, identified by the radio continuum maps with $\sim 2''$ beam presented by J. M. Cannon et al. (2005); they also include the peaks of the ^{12}CO(2–1) detection near the NW OB association by L. Zhou et al. (2021), and the ultraluminous X-ray source ULX-1 found by T. X. Thuan et al. (2004). In addition, we placed apertures on the approximate centers of the NW and SE OB complexes.

Finally, from visual inspection along the wavelength planes of the MIRI spectral cube, besides VLA-NW-A, which appears as a continuum source, we noticed three additional continuum sources near the VLA-SE H II region, although not exactly coincident with it. Apertures for spectral extraction were also placed on the 14 μm peaks of this emission, as measured from the cube; these are denoted as JWST-SE-1, JWST-SE-2, and JWST-SE-3. These continuum sources are also apparent in the MIRI images presented by A. S. Hirschauer et al. (2024), and will be discussed in Section 4. Table 1 reports the aperture centers used here.

The aperture size is designed to encompass at least 65% of the light in the PSF of the convolution kernel. J. Rigby et al. (2023) found that an aperture of 0.″64 radius encloses 65% of the energy in the F2550W MIRI filter,[24] similar in wavelength to the 27 μm kernel. Although a larger aperture would be desirable, it results in incomplete spectra in several of the regions of interest, because of the smaller field of view (FOV) at shorter wavelengths. Thus, we adopt an aperture with radius 0.″65 as a compromise. Moreover, in order to reduce sampling artefacts in the recovered spectra, D. R. Law et al. (2023) recommended an extraction diameter at least equal to the FWHM of the PSF. Since the [O IV] wavelength in MIRI/MRS has a PSF FWHM $\sim 0.''96$ (Equation (1) in D. R. Law et al. 2023), the adopted diameter of 1.″3 satisfies this recommendation even for the longest wavelength of interest. Because we cannot know a priori whether or not the emission

[24] See also https://jwst-docs.stsci.edu/jwst-mid-infrared-instrument/miri-performance/miri-point-spread-functions#gsc.tab=0.

Table 1
Aperture Centers for Spectral Extraction

Region	R..A. (J2000)	Decl.
NW	9:34:01.99	+55:14:27.3
VLA-NW-A	9:34:02.10	+55:14:28.1[a]
VLA-NW-B	9:34:01.85	+55:14:26.0[a]
VLA-NW-C	9:34:01.82	+55:14:29.1[a]
ULX-1	9:34:01.97	+55:14:28.4[b]
CO2-1	9:34:02.00	+55:14:28.8[c]
SE	9:34:02.29	+55:14:23.5
VLA-SE	9:34:02.36	+55:14:23.1[a]
JWST-SE-1	9:34:02.31	+55:14:24.1
JWST-SE-2	9:34:02.36	+55:14:22.6
JWST-SE-3	9:34:02.18	+55:14:23.2

Notes.
[a] J. M. Cannon et al. (2005);
[b] T. X. Thuan et al. (2004); J. Ott et al. (2005); R. J. Rickards Vaught et al. (2021);
[c] L. Zhou et al. (2021).

is unresolved (pointlike) or extended, an aperture of constant size across wavelength was deemed the best option.

The apertures are shown in the bottom-right panel of Figure 1, where we have overlaid in red the three MIRI images, F560W, F1130W, and F2550W, on the HST F606W image, shown in blue. Clearly, the apertures are not independent. However, our objective is not to sample independent regions, but rather a variety of individual regions to assess differences in ionization state. The reddish/purple hue of the environment of the SE OB complex in Figure 1 indicates that it has more warm dust than the NW in general, with the exception of the VLA-NW-A HII region. The curved gaseous filaments around the NW OB complex are clearly visible, appearing also in the F560W image, resulting in a purple color.

The spectra extracted from the convolved cubes are shown in Figure 2, with offsets to enhance the visibility of the individual spectra. For each spectrum, the light-gray curves show the original spectra, and the thick colored curves show the smoothed continuum, as reported in the legend; the horizontal dotted colored lines show the zero level for each spectrum.

Emission lines were identified with an automatic algorithm based on `find_lines_threshold` within `Astropy/specutils` (N. Earl et al. 2020). The fits to the piece-wise smoothed continuum were subtracted from the observed spectra, and the noise in the individual spectral regions was estimated for input to the line-finding algorithm, by calculating the standard deviation in the piece-wise smoothed continuum with `noise_region_uncertainty`. Potential line detections were defined with an initial signal-to-noise ratio (S/N) threshold of 3. Each of these potential detections was then fit with the sum of a Gaussian and a linear continuum in a window around the potential line. Lines were identified by comparing the rest-frame wavelength of the best-fit Gaussian with known line lists (B. T. Draine & F. Bertoldi 1996; P. A. M. van Hoof 2018). The total line flux was calculated by integrating the Gaussian, and flux uncertainties by propagating the errors on the fitted parameters given by the Hessian matrix associated with the fit. Finally, we extracted the list of detected lines by requiring an $S/N = 3$ on the fitted flux, and the absolute value of the velocity offset to be $\leqslant 250\,\mathrm{km\,s^{-1}}$. A subset of these is shown in Figure 2 as vertical dotted lines.

In I Zw 18, the MIRI 1D spectra show ($S/N \geqslant 3$) detections for a total of 10 fine-structure (FS) lines, 15 H I recombination lines, and seven H_2 transitions. Table 2 gives the ionization potentials to create the corresponding ions (IPs) for the FS lines detected in the MIRI spectra of I Zw 18. The detected ionized-line fluxes and their uncertainties are reported in Appendix B in Tables 5 and 6. The Gaussian fits to the [O IV] and [Ne V] are also shown in Appendix B in Figures 11 and 12. In this paper, we restrict the discussion to the ionized gas; the warm H_2 and the dust emission in aperture spectra are described in a companion paper (Paper II).

3. Ionized Gas

The ionized gas in I Zw 18 is in an extremely high-ionization state. MIRI significantly detects [O IV] within eight apertures and the high-ionization line [Ne V] 14.32 in four (which can be mapped; L. K. Hunt et al. 2025, in preparation). Although [Ne V], with an IP of 97.1 eV, is detected at optical wavelengths ([Ne V] λ3426) in several BCDs (e.g., T. X. Thuan & Y. I. Izotov 2005; Y. I. Izotov et al. 2012), it has not yet been detected in I Zw 18 in the optical (e.g., Y. I. Izotov et al. 2021), perhaps because of insufficient spatial or wavelength coverage.

The [Ne V] 24.32 line is not detected, but we can use the upper limits (ULs) on the line flux to investigate the electron density n_e in the four regions where [Ne V] 14.32 is detected: CO2-1, NW, VLA-NW-A, ULX-1. The 3σ ULs for [Ne V] 24.32 are, respectively, $2.4 \times 10^{-20}\,\mathrm{W\,m^{-2}}$, $8.5 \times 10^{-21}\,\mathrm{W\,m^{-2}}$, $1.6 \times 10^{-20}\,\mathrm{W\,m^{-2}}$, $3.1 \times 10^{-20}\,\mathrm{W\,m^{-2}}$, corresponding to ULs on [Ne V] 24.32/[Ne V] 14.32 (see Table 5) of $\lesssim$7 (CO2-1), $\lesssim$1 (NW), $\lesssim$2 (VLA-NW-A), and $\lesssim$8 (ULX-1). The line ratio is expected to vary from $\sim$1 for $n_e < 10^3\,\mathrm{cm^{-3}}$ to $\sim$0.1 for $n_e > 10^5\,\mathrm{cm^{-3}}$ (B. T. Draine 2011). Thus, the present upper limits for [Ne V]24.32/[Ne V]14.32 do not constrain n_e.

3.1. Extinction from H I Recombination Lines

We have investigated the internal extinction in the aperture spectra using the H I recombination lines given in Table 3, combined with those taken from the KCWI (see Section 2.1; R. J. Rickards Vaught et al. 2021). An S/N of 10 was adopted for the individual detections to maximize the reliability of the measurements. To calculate the intrinsic line ratios, we relied on Case B emissivities from `PyNeb` (V. Luridiana et al. 2015), fixing the electron temperature to $T_e = 20{,}000$ K and the electron density to $n_e = 100\,\mathrm{cm^{-3}}$ (Y. I. Izotov et al. 1999; C. Kehrig et al. 2015).

We experimented with two extinction curves, J. C. Weingartner & B. T. Draine (2001, hereafter WD01) and K. D. Gordon et al. (2023, hereafter G23),[25] as implemented in `dust-extinction`,[26] an affiliated package of `Astropy`. Several trials were run using only the MIRI H I lines to infer extinction, but the extinction is so small that the uncertainties are too large to be reliable. Thus, we have compared the MIRI lines to Hβ, as shown in Figure 3. There are negligible

[25] The G23 extinction curve also incorporates results by K. D. Gordon et al. (2009), E. L. Fitzpatrick et al. (2019), K. D. Gordon et al. (2021), and M. Decleir et al. (2022).
[26] Available at https://dust-extinction.readthedocs.io/en/stable/ (K. Gordon 2024).

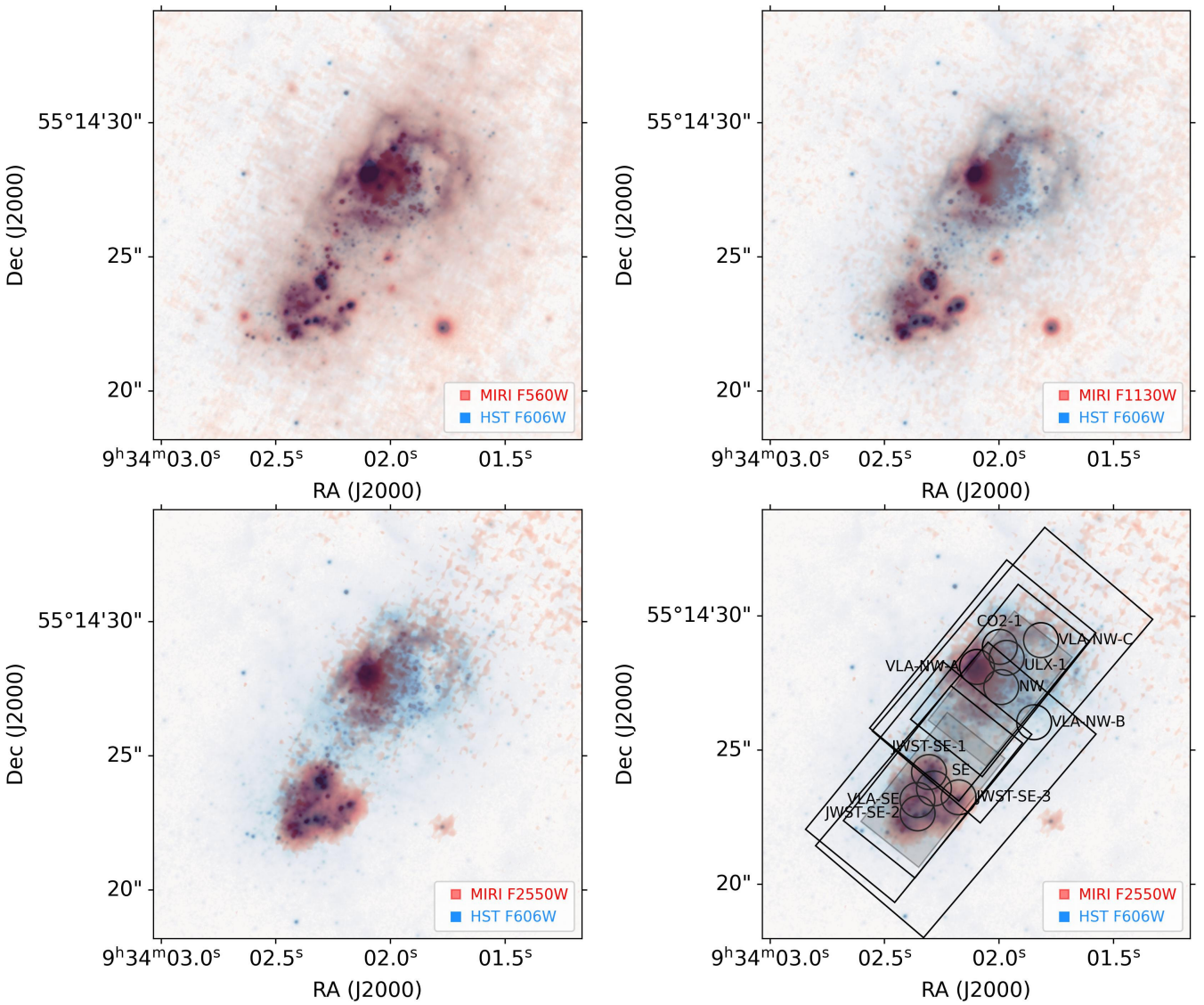

Figure 1. 16″ × 16″ overlays of MIRI images of I Zw 18 on the HST F606W image astrometrically corrected to Gaia. The MIRI F560W filter is shown in the top-left panel, and F1130W is shown in the top-right panel. The F2550W filter appears in the bottom panels, with the MIRI fields of view (FOVs) from both pointings in the four overlapping channels overlaid in the right panel, together with the circles giving the apertures (0.″65 radius, ∼120 pc diameter) for spectral extraction. The smallest FOV of Channel 1 is indicated by a slightly opaque background. The underlying HST image is illustrated in bluish tones, while the MIRI images are shown in reddish ones.

differences between results from the WD01 and the G23 extinction curves, so we illustrate only G23.

Figure 3 plots as a function of wavelength the G23 extinction inferred relative to Hβ from KCWI for the H I recombination lines detected with S/N $\geqslant$ 10 in the apertures defined in Section 2.2 (Table 1). VLA-NW-B and VLA-NW-C are not shown because they do not fall within all of the MIRI channels. We have checked whether He II lines could be potentially blended with the H I lines (e.g., Huα), and thus the flux overestimated; however, no evidence was found for asymmetric line profiles with a blue shoulder, as would be expected if this were the case. Thus, the mid-infrared (MIR) H recombination-line fluxes should not be significantly contaminated by He II.

Figure 3 shows that the extinction in I Zw 18 is small (foreground extinction has not been corrected for and will be discussed below). The gray regions and mean $\langle A_V^{\rm IR} \rangle$ values and spreads given in the top-left corner of each panel are calculated using only MIRI lines. We have done this to assess if the optical were unable to penetrate deeply embedded sources (e.g., D. Calzetti et al. 1994; L. K. Hunt et al. 2001); however, there is no systematic dependence on MIR wavelength that might be expected if this were true. Nevertheless, A_V inferred from the optical is ∼0.1–0.2 mag lower than the MIR estimates in the three JWST-SE continuum and SE apertures (but not in VLA-SE). The extinction measured by MIRI is highest in JWST-SE-2, $A_V \sim 0.3$, although it is not similarly high in all of the SE apertures. In VLA-NW-A, the optically inferred A_V lies ∼0.2 mag above the MIRI values, which are significantly negative. After tests, we find that the inferred MIR extinction would be roughly zero, if, for that aperture, we assume a higher T_e (∼24,000–25,000 K) and a higher electron density to n_e ($\sim 10^4$ cm^{-3}), consistent with the higher temperatures and dense gas located near VLA-NW-A found by Rickards Vaught et al. (2025, Paper III).

The extinction measured in I Zw 18 is comparable with that estimated for the foreground, due to dust in the Milky Way.

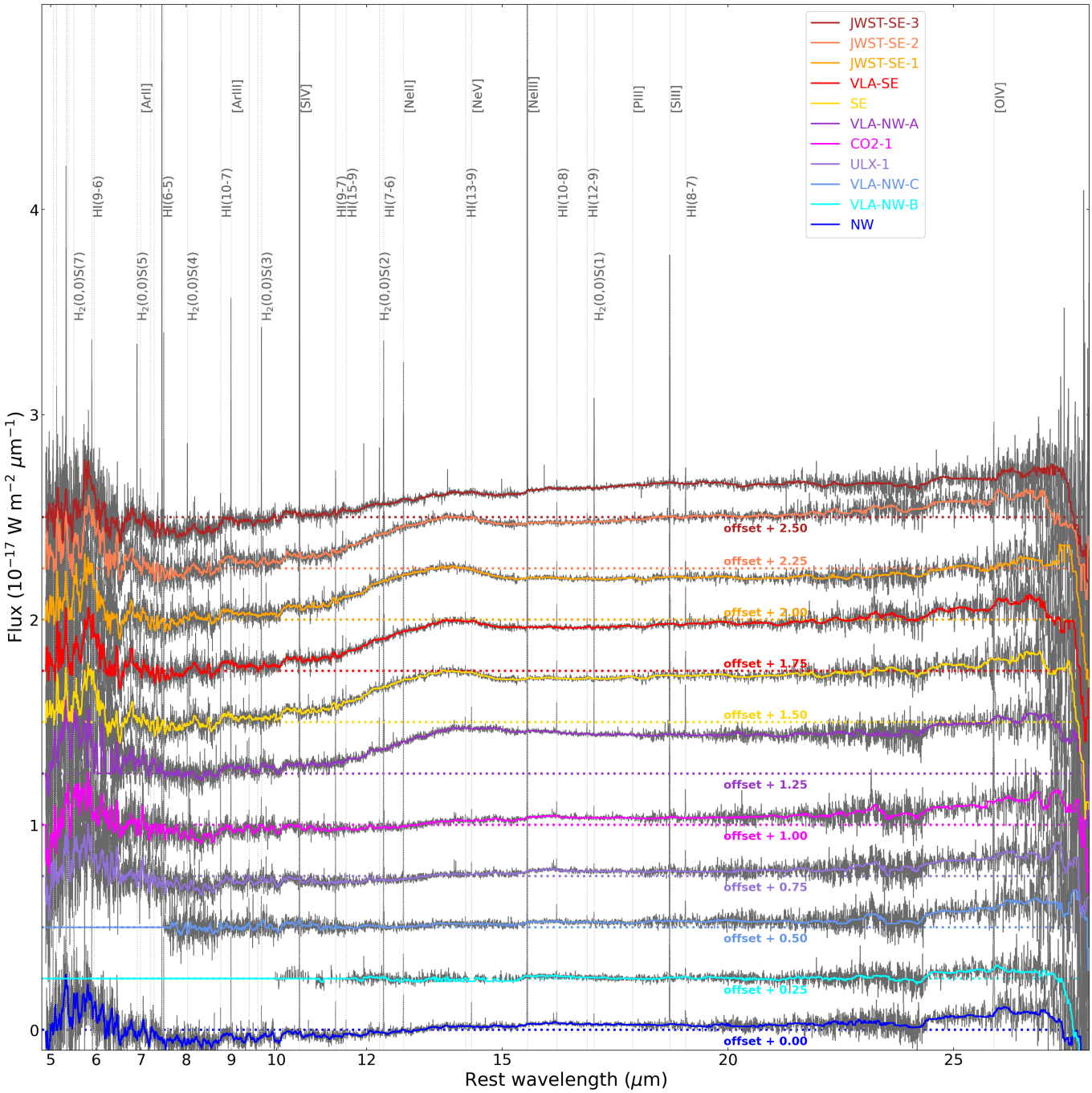

Figure 2. Spectra extracted the 27 μm convolved cubes in the 0.″65-radius apertures shown in Figure 1. The vertical axis for flux density is in units of 10^{-17} W m^{-2} μm^{-1}, and the horizontal wavelength axis in microns. The gray curves show the spectra, while the thick colored curves show the smoothed continuum; the dotted horizontal colored lines indicate the zero level of the spectra. For better visibility, the spectra are offset by small increments (in the vertical-axis units of 10^{-17} W m^{-2} μm^{-1}), as denoted in the figure. The vertical dotted lines correspond to the detected transitions given in Tables 5 and 6; to avoid overcrowding, not all lines are labeled. The spectra for VLA-NW-B and VLA-NW-C are missing the short-wavelength MIRI channels because part of the aperture falls outside the MIRI FOV at those wavelengths.

Foreground extinction for each aperture was determined from the D. J. Schlegel et al. (1998) dust maps recalibrated to the scale of E. F. Schlafly & D. P. Finkbeiner (2011), as implemented in the publicly available Python package `dustmaps`[27] (G. Green 2018). For a given location on the sky, the module returns the corresponding $E(B-V)$ value derived by linearly interpolating the dust maps; $R_V = 3.1$ was used to convert $E(B-V)$ to A_V. This process was reproduced for each of the 11 apertures considered, but there is very little variation (a standard deviation of ± 0.0001 over the 11 apertures, presumably because of the low spatial resolution of the dust maps). We find a mean foreground extinction for I Zw 18, $A_V = 0.091$, in agreement with the A_V value from E. F. Schlafly & D. P. Finkbeiner (2011) tabulated by NED.

[27] `dustmaps` is found at https://dustmaps.readthedocs.io/en/latest/maps.html and the dust maps themselves can be accessed and downloaded in the context of this package.

Table 2
Detected FS lines[a]

Line	Rest Wavelength (μm)	Ionization Potential (eV)
[Ar II]	6.98527	15.76
[Ar III]	8.99138	27.63
[Fe II]	5.34017	7.90
[Ne II]	12.81355	21.56
[Ne III]	15.55510	40.96
[Ne V]	14.32170	97.12
[O IV]	25.89030	54.93
[P III][b]	17.88500	19.77
[S III]	18.71300	23.34
[S IV]	10.51050	34.79

Notes.
[a] Wavelengths and IPs taken from P. A. M. van Hoof (2018) and https://www.mpe.mpg.de/ir/ISO/linelists/FSlines.html.
[b] Possible weak detection only in aperture VLA-NW-A.

Table 3
MIRI H I Lines Used for Extinction Calculations[a]

Line	Rest Wavelength (μm)
Huγ H I 9–6	5.90821
Pfα H I 6–5	7.45986
Huβ H I 8–6	7.50249
H I 10–7	8.76006
H I 9–7	11.30870
H I 15–9	11.53949
Huα H I 7–6	12.37190
H I 10–8	16.20910
H I 12–9	16.88063
H I 8–7	19.90619

Note.
[a] These are the H I detections with S/N $\geqslant$ 10 in the aperture spectra, as discussed in the text.

Thus, it is probable that the extinction in I Zw 18 is so low as to be extremely difficult to measure against the foreground, even leveraging the large wavelength coverage provided here.

The inferred A_V also depends on the method for determining foreground extinction. Using the Planck extinction maps (Planck Collaboration et al. 2016), the estimated foreground extinction $A_V = 0.137$, larger than the $A_V = 0.091$ that we measure, so most of the extinction in I Zw 18 would be attributed to Milky Way dust. Because of the small value and large scatter for the internal extinction in I Zw 18, none of the emission lines studied here have been corrected for dust.

Figure 2 suggests that there may be greater dust content in the SE. Warm dust, evident in the emission bump around 14 μm, appears not only in the brightest H II region, VLA-NW-A, but also in the SE, around the HII region VLA-SE, the SE OB complex, and the JWST-SE continuum sources. This is a qualitative confirmation of what is seen also in Figure 1. From Figure 3, we can compare the inferred extinction in the NW to that in the SE. The extinction averaged over all of the NW regions is $A_V = 0.07$ (where VLA-NW-A is taken to have $A_V = 0$), and in the SE, mean $A_V = 0.12$. Such a difference is negligible, and within estimates of foreground extinction, but may hint of more dust in the SE, as also found by J. M. Cannon et al. (2002) using narrowband Hα and Hβ HST images.

3.2. Fine-structure Line Ratios

The hardness[28] of the RF is an important diagnostic to determine the dominant energy source powering the ionizing radiation. It is well established that the effective hardness of the stellar RF increases with decreasing metallicity (e.g., A. Campbell et al. 1986; J. M. Vilchez & B. E. J. Pagel 1988). Because of this, [O IV] with an IP of 54.9 eV just beyond the He II edge, has been frequently detected in BCDs (Y. Wu et al. 2007; L. Hao et al. 2009; L. K. Hunt et al. 2010). However, only with JWST/MIRI is it possible to detect even higher ionization MIR lines such as [Ne V]. Before JWST, no BCD has been clearly detected in the [Ne V] 14.32 μm line. Now, in addition to I Zw 18, [Ne V] 14.32 has also been detected in another metal-poor BCD, SBS 0335−052, at ∼5% solar, slightly more metal-rich than I Zw 18 (M. Mingozzi et al. 2025). JWST is also detecting such high-ionization lines in more massive star-forming galaxies (e.g., M83; S. Hernandez et al. 2025), and is expected to revolutionize our perspective on high-ionization emission lines in star-forming galaxies.

Because of their different IPs (see Table 2), [Ne III]/[Ne II] and [S IV]/[S III] flux ratios trace the hardness of the RF (e.g., M. D. Thornley et al. 2000; E. Sturm et al. 2002; A. Verma et al. 2003). Combining lines with even larger differences in ionization potentials can distinguish between accreting massive black holes (or active galactic nuclei, AGN) and stellar sources, although fast radiative shocks can sometimes mimic AGN, particularly in low-metallicity environments (e.g., Y. I. Izotov et al. 2012, 2021). Figure 4 shows three commonly used diagnostics of the hardness of the RF plotted against [Ne III]/[Ne II]. The line ratios from the MIRI apertures for I Zw 18 are shown as filled stars, as described in the legend in the top-right panel.

To place I Zw 18 in the context of the broader galaxy population, we have included for comparison other BCDs (L. Hao et al. 2009; L. K. Hunt et al. 2010), star-forming galaxies (A. Verma et al. 2003; S. Satyapal et al. 2008; J. Bernard-Salas et al. 2009; D. A. Dale et al. 2009), luminous infrared galaxies (LIRGs) from the Great Observatories All-sky LIRG Survey (GOALS; H. Inami et al. 2013), galaxies hosting AGN (E. Sturm et al. 2002; D. W. Weedman et al. 2005), and AGN in dwarf galaxies (C. E. Hood et al. 2017). Indicated in the top panels are also previous MIR observations of I Zw 18 (Y. Wu et al. 2007), and two other BCDs (roughly 10 times more metal-rich than I Zw 18), II Zw 40 and NGC 5253 (A. Verma et al. 2003).

Because I Zw 18 is known to harbor Wolf–Rayet (WR) stars, particularly in the NW (F. Legrand et al. 1997; Y. I. Izotov et al. 1997; D. Schaerer et al. 1999; T. M. Brown et al. 2002), we also include in the comparison sample the WR nebula N76 (Y. Nazé et al. 2003; E. Tarantino et al. 2024) in the Small Magellanic Cloud (SMC, ∼20% solar metallicity). The central ionizing source, AB7, is one of the most luminous WR stars in the SMC, and provides a useful template for the ionization properties of an extreme stellar source, able to create a highly ionized H II region. Models of hot, low-metallicity sources like AB7 suggest that they contain sufficient numbers of high-energy photons to produce considerable [O IV] and [Ne V] emission (D. Schaerer & W. D. Vacca 1998; D. Schaerer & G. Stasińska 1999). E. Tarantino et al. (2024) reported detections from Spitzer/IRS

[28] By hardness, we mean the slope of the 13.6–100 eV RF spectrum.

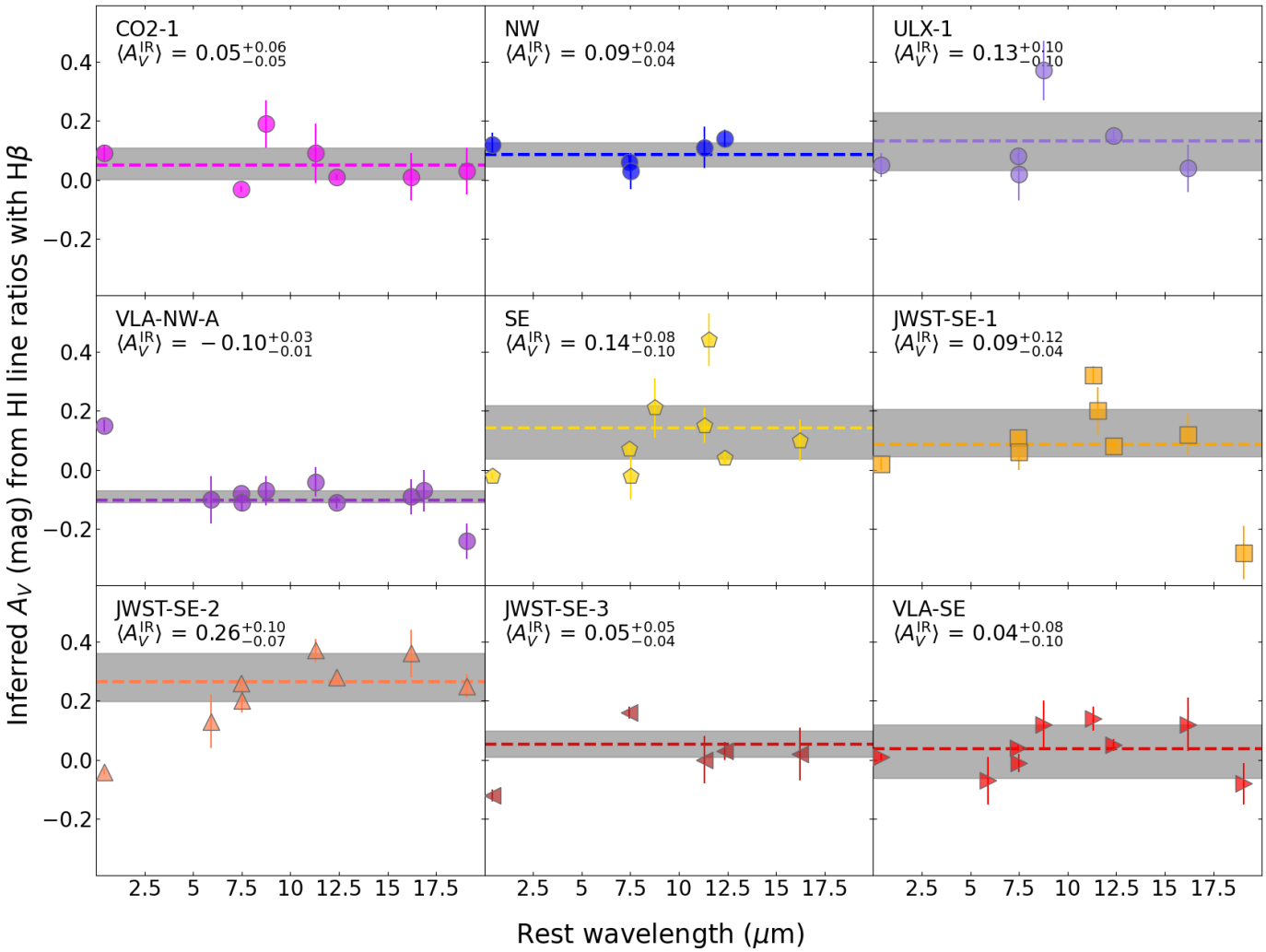

Figure 3. Inferred extinction relative to Hβ using Hδ from KCWI, and the detected MIRI H I recombination lines with an S/N $\geqslant$ 10; G23 is assumed for the extinction curve, and no foreground extinction has been applied. The extinction values for each aperture are plotted against the wavelength of the MIRI H I lines to illustrate the power of the MIRI wavelengths to probe deeper into embedded regions. The horizontal shaded light-gray rectangles in each panel show the 1σ spread of the ensembles. The A_V values in the top-left corner of each panel correspond to the MIRI average and spread, not taking into account the optical Hδ/Hβ values. VLA-NW-B and VLA-NW-C are not shown because they are not uniformly within the FOV of the individual MIRI channels (see Figure 1).

observations of all of the ionized-gas lines studied here. However, they detected [Ne V] 24.32 rather than [Ne V] 14.32; therefore, in the relevant plots, we divide the [Ne V] 24.32 flux by factors of 1 and 0.1, corresponding to the low- and high-density limits, respectively, of the [Ne V] 24.32/[Ne V] 14.32 line ratio (see above and B. T. Draine 2011).

A clear correlation between [S IV]/[S III] and [Ne III]/[Ne II] can be seen in the top panels of Figure 4, similar to previous studies (e.g., L. Hao et al. 2009); our MIRI observations of the individual regions within I Zw 18 are consistent with these trends at the extreme high-ionization end. The similarity of these line ratios for galaxies with known AGN or composites with SF+AGN contributions implies that the IPs of these lines are insufficiently high to be diagnostic of extremely hard ionizing radiation. Higher ionization lines are needed, as we show in the middle and bottom panels.

The middle panels of Figure 4 show [O IV]/[S III] versus [Ne III]/[Ne II]. Some of the observations shown in the top panels have not been included (e.g., Y. Wu et al. 2007; J. Bernard-Salas et al. 2009), because the galaxies tend to fill the spectroscopic slits, and the different Spitzer/IRS LH ([O IV]) and SH ([S III], [Ne III], [Ne II]) slit sizes have not been corrected for. The NW regions in I Zw 18 are apparently in a higher ionization state than in the SE; the SE regions fall on the extension of the trend of earlier observations, while in the NW, the ratios are significantly above the [O IV]/[S III] trend and also have the highest [Ne III]/[Ne II] values. As also found by L. Hao et al. (2009) for [O IV] 25.89/[S III] 33.48, there appear to be two different sequences for [O IV]/[S III] relative to [Ne III]/[Ne II], namely an SF sequence and an AGN one with higher [O IV]/[S III] for a given [Ne III]/[Ne II] ratio. The dotted–dashed lines indicating the locus of the "SF sequence" and "AGN sequence" are merely to guide the eye; no formal fitting procedure has been applied.

The bottom panels show the higher ionization line [Ne V] ratio with [Ne II]. The galaxy indicated in the bottom panel, NGC 3938, is a giant spiral in which [Ne V] was unexpectedly detected (S. Satyapal et al. 2008). The high [Ne III]/[Ne II] portion of the plot is occupied by this galaxy, the SMC N76 WR, and the four regions in the NW of I Zw 18 where [Ne V] is detected. These points clearly fall below and to the right of the trend shown by the AGN. Here also, as for [O IV], there may be two kinds of behavior, reflecting different sources of ionization for the emission.

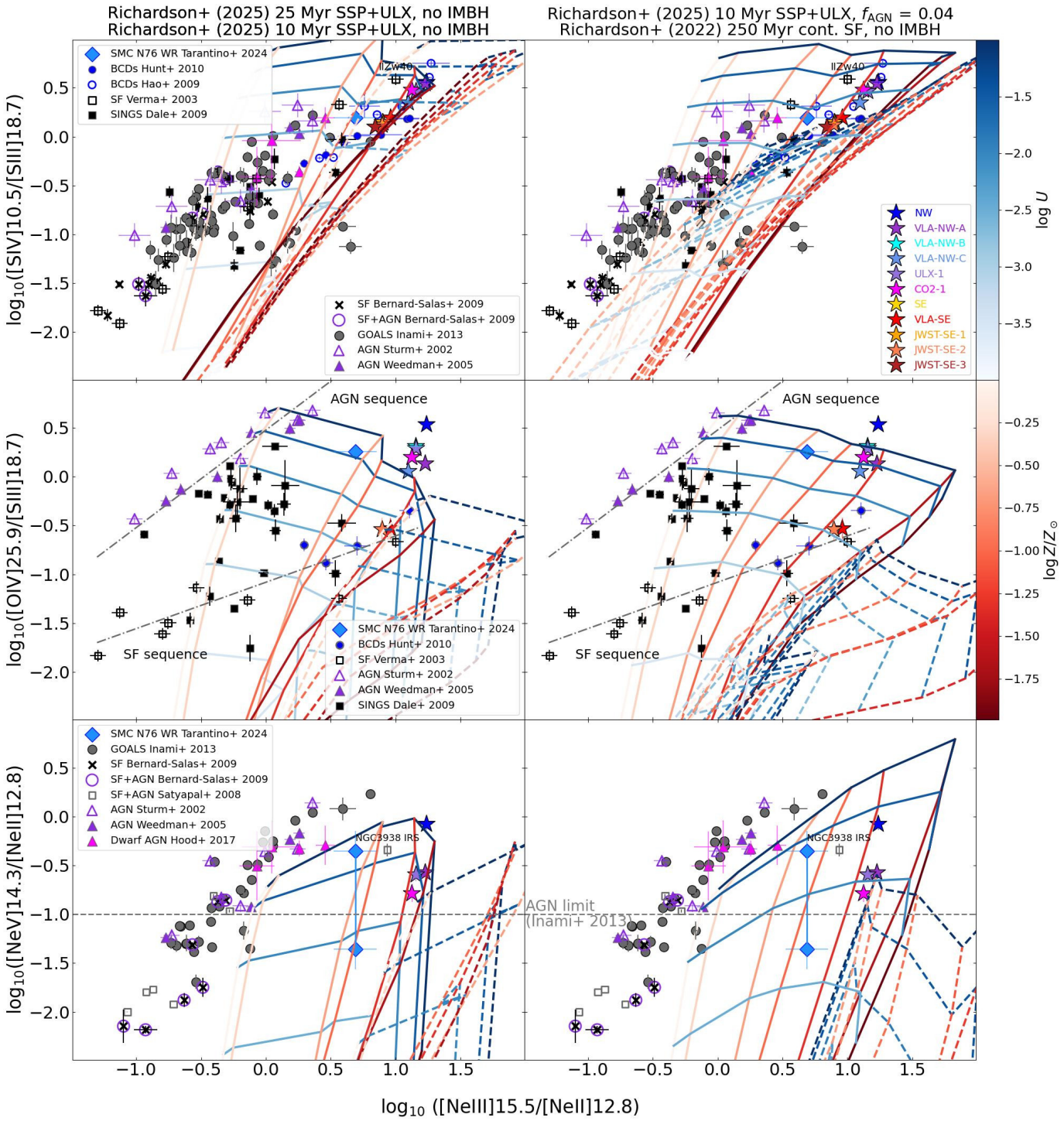

Figure 4. Comparison of various RF diagnostic line flux ratios plotted vs. [Ne III]/[Ne II]. Top panel: [S IV]/[S III]; middle: [O IV]/[S III]; bottom: [Ne V]/[Ne II]. Our MIRI points for I Zw 18 are given as stars, shown in the legend in the top-right panel. Other samples of galaxies, AGN, BCDs, and dwarf galaxies with AGN are shown in the legends according to the line ratio. When the error bars are not evident, they are smaller than the symbol. In the middle panel, an "AGN sequence" and an "SF sequence" are illustrated by dotted–dashed lines. In the bottom panel, the horizontal dashed line corresponds to the AGN criterion of [Ne V]/[Ne II] $\geqslant 0.1$ defined by H. Inami et al. (2013). The same data are plotted in each row, but the left panels show the model grids by R25, where the 10 Myr simple stellar populations (SSPs) are given with dashed contours, and the 25 Myr SSPs are given with solid ones. The right panels show the 250 Myr continuous star formation (CSF) population from R22 given as dashed curves, and, as solid ones, the R25 model with $f_{AGN} = 0.04$ and a post-starburst age of 10 Myr. The color maps for the model grids for $\log(U)$ and $\log(Z/Z_{\odot})$ are the same for all models.

While the SMC N76 WR from E. Tarantino et al. (2024) is indistinguishable from the general trends in the [S IV]/[S III] and [Ne III]/[Ne II] line ratios, it stands out as one of the extreme sources in [O IV]/[S III] and [Ne V]/[Ne II]. In these line ratios, it is similar to the NW apertures in I Zw 18, although with slightly lower [Ne III]/[Ne II]. The shape of N76, powered by the WR/O-star binary AB7, is an approximately spherical shell, of ∼40 pc in radius, while the highly ionized gas, [O IV] and [Ne V], also has a shell-like morphology, but is smaller, with a projected radius of

10–20 pc. A WR binary like AB7 in the SMC could be powering some of the photoionization in I Zw 18; we will discuss this point further below.

3.3. Comparison with Models

Figure 4 also illustrates a comparison with model grids. The goal of this comparison is two-fold: (1) to assess the success of the models to encompass the line ratios of a wide variety of galaxies; and (2) to compare the models in particular to I Zw 18 to constrain the excitation mechanisms. This broader comparison enables a sanity check for the general viability of the models, and thus, their applicability to I Zw 18. The left panels show selected simple stellar population (SSP) models from C. T. Richardson et al. (2025, hereafter R25), where we have not included any contribution from the accreting intermediate-mass black holes (IMBHs)[29] also modeled by them (for the left panels, we assume an AGN fraction $f_{\rm AGN} = 0$). The panels on the right show the stellar populations associated with a continuous star formation (CSF) history at an age of 250 Myr by C. T. Richardson et al. (2022, hereafter R22). They also include R25 models with a small contribution from an IMBH as described below.

Both sets of models rely on the Binary Population and Spectral Synthesis (BPASS) code (E. R. Stanway et al. 2016; J. J. Eldridge et al. 2017) that considers stellar binary evolution, spanning a range of ages; the R22 models comprise metallicities from $0.05\,Z_\odot$ to $Z_\odot$, while R25 models comprise metallicities from $0.01\,Z_\odot$ to $Z_\odot$. In R22 and R25, these stellar continua photoionize gas with ionization parameters $\log \mathcal{U}$ ranging from -4 to -0.5.

The R25 models also include self-consistent contributions from XRBs in the form of ULXs as a function of age and stellar population metallicity, as first implemented by K. Garofali et al. (2024). ULXs are a luminous subclass of XRBs that comprise a high-mass donor star undergoing mass transfer and accretion onto a compact object, assumed to be a stellar-mass BH in the models. ULXs can therefore establish an upper limit to X-ray excitation in the case where there is no IMBH. This is important, in particular, for I Zw 18 which contains ULX-1 (T. X. Thuan et al. 2004; P. Kaaret & H. Feng 2013). The combination of the SSP+ULX SED models, which considers the timing of the onset of high-mass XRBs, and the effects of metallicity on stellar evolution and stellar wind properties, should ensure an overall realistic and self-consistent stellar population. In these models, the shape of the ULX photoionizing SED does not vary with time, but the normalization does; metallicity affects both the SED shape and normalization.

As shown in Figure 5, where the ionizing SEDs are plotted as a function of energy, age regulates the normalization relative to the remaining stellar populations. Lower metallicity makes the ionizing SED harder (solid versus dashed curves), and at 25 Myr, the ULX contribution is maximized, relative to the stellar component (red curves). Unlike the R22 models, the R25 models include a ULX population in addition to the SSPs (e.g., K. Garofali et al. 2024); this results in significant ionizing flux at energies $\gtrsim 50$ eV. This behavior is reflected in the right panels of Figure 4, where the R22 models without an IMBH are not able to reproduce the high [O IV]/[S III], while the R25 models without an IMBH in the left panel do a better job at reproducing this ratio.

Figure 5 also compares the best-fit composite model SED of the WR binary AB7[30] exciting SMC N76 (T. Shenar et al. 2016). It provides an ionizing flux similar to the most extreme SSP+ULX at ~50 eV, consistently with the observed high-ionization emission lines, [Ne V] and [O IV], observed by E. Tarantino et al. (2024) in this object and shown in Figure 4.

For completeness, we have included in the model comparison the R25 model of an SSP+ULX at 10 Myr where the ULX contribution is ~10 times lower relative to the SSP than the maximum at 25 Myr (see Figure 5), but with an AGN fraction $f_{\rm AGN}$ of 4%; the "AGN fraction" $f_{\rm AGN}$ corresponds to the fraction of ionized photons attributed to the AGN. We have assumed the "light seeding" scenario; see R25 for more details.[31] This is a relatively arbitrary choice, but the aim here is to illustrate the trends of the models with low $f_{\rm AGN}$. The right panels of Figure 4 shows these model grids, illustrating that they are very similar to the maximum ULX contribution at 25 Myr (shown in the left panel). This is due to the resemblance of the photoionizing SEDs in Figure 5. Such ambiguity makes it difficult to make decisive claims about the need for an IMBH (or not) in I Zw 18.

In general, the R25 models are fairly successful at reproducing the line ratios of the broader galaxy population. The model grids show that increasing [S IV]/[S III] is associated with increasing $\log \mathcal{U}$, and increasing [Ne III]/[Ne II] with decreasing Z (see color maps for the models in the right panels, the same for all panels in the plot). [O IV]/[S III] also increases with decreasing Z as expected, and with increasing $\log \mathcal{U}$. Moreover, the 25 Myr models, with the maximum ULX contribution and the highest ionization parameter U come very close to matching the line ratios of I Zw 18 (left panels of Figure 4). This is particularly true for the [Ne V]/[Ne II] ratio of I Zw 18 (bottom panel of Figure 4), where the most metal-poor model curves with the highest U are coincident with what is observed in I Zw 18. However, without an IMBH, the R22 CSF models lie somewhat far from the [Ne V]/[Ne II] ratios of observed AGN and some of the LIRGs, mainly because the [Ne III]/[Ne II] ratios tend to be somewhat overpredicted.

The measured line ratios may reflect additional physical phenomena (e.g., shocks) that are not described by photoionization models. Thus, in Figure 6, we examine the shock models by S. R. Flury et al. (2024, hereafter F24). These are based on MAPPINGS V (R. S. Sutherland & M. A. Dopita 2017; R. Sutherland et al. 2018), treating shocks as a time-dependent flow in the frame of the shock. The precursor gas, the gas upstream of the shock, has a given ionization balance, density, temperature, and composition. The shock front is characterized by a velocity and magnetic field strength, B, and gas beyond the shock front is collisionally excited to very high temperatures ($T \sim 10^6$ K; e.g., L. Binette et al. 1985; B. T. Draine & C. F. McKee 1993; R. S. Sutherland & M. A. Dopita 2017). As this gas cools, high-ionization species such as [Ne V] can persist in the gas even as it approaches lower temperatures ($T \sim 10^4$ K). For more details, see F24. Metallicities in the models range from $\log(Z/Z_\odot)$ −1.3 to 0.3,

[29] IMBHs, by definition, have masses from $\sim 100\,M_\odot$ to $\sim 10^5\,M_\odot$ (e.g., A. K. Bhowmick et al. 2024).

[30] We show the sum of the two separate components, WR+O6.

[31] The seeding mechanisms in R25 have a metallicity dependence; for light seeding, the IMBH masses range from $100\,M_\odot$ at the lowest metallicity to $10^{5.89}\,M_\odot$ at the highest.

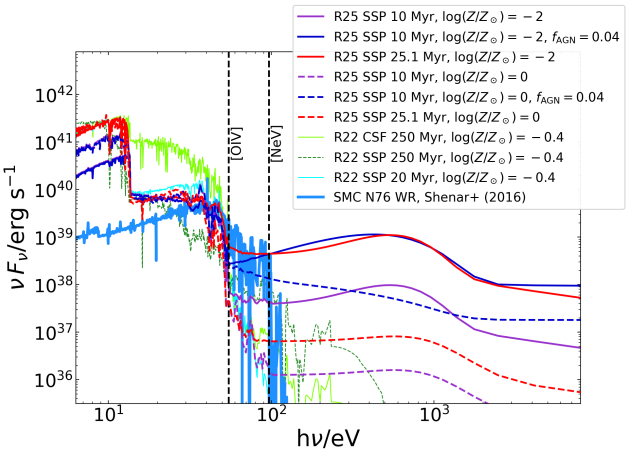

Figure 5. SEDs of selected R22 and R25 SSP+ULXs plotted against photon energy in eV. These R25 populations have ages of 10−25 Myr, and two values of metallicities: $\log(Z/Z_{\odot}) = -2$ and $\log(Z/Z_{\odot}) = 0$. The addition of $f_{\rm AGN} = 0.04$ to the R25 10 Myr SSP+ULX at the same two metallicities is also shown, together with the SEDs of the stellar populations modeled by R22, at two ages (SSPs with 20 Myr, 250 Myr; CSF 250 Myr) with a single, intermediate, metallicity, $\log(Z/Z_{\odot}) = -0.4$. The best-fit composite model SED of the WR/O binary star AB7 in the SMC is also shown (T. Shenar et al. 2016). The IPs necessary to produce [O IV] and [Ne V] are illustrated as dashed vertical lines.

so may not be strictly appropriate for I Zw 18; nevertheless, our goal is to assess the differentiation of shocks from photoionization with data spanning the broader galaxy population.

In Figure 6, the color maps indicate metallicity and shock velocity, and we have limited the plots to pre-shock densities of 10 $\rm cm^{-3}$, but checked that this parameter is not crucial for defining the range in predicted line ratios (see also R25). In the left panel, the magnetic field B has a value of 10 μG, the highest value modeled by F24, and in the right panel, 10^{-4} μG, the lowest. The highest B field tends to be more successful than the lowest in reproducing the overall trends in the line ratios, in particular for [O IV]/[S III] (middle panel of Figure 6). Shocks are also able to reproduce the observed range of [Ne V]/[Ne II] versus [Ne III]/[Ne II] for the overall galaxy populations (bottom panel), but not for I Zw 18, which seems to be better approximated by the SSP+ULX populations of R25 (or the light-seed $f_{\rm AGN} = 0.04$).

Finally, in Figure 7, we compare a different set of line ratios with models. These line ratios, [O IV]/[Ne III] combined with [Ne III]/[Ne II] and [S IV]/[Ne II], are proposed by R25 to be the strongest diagnostics for separating stars+ULX and AGN contributions. The R25 models shown in Figure 4 are also given in the left panels (no IMBH), and in the right, the R22 (no IMBH) and the R25 10 Myr light-seed model with $f_{\rm AGN} = 0.04$. The two F24 shock models from Figure 6 are also given in the right with the same color coding as in Figure 6. The demarcation lines correspond to Equations (9) and (10) in R25, as well as the vertical line corresponding to an [O IV]/[Ne III] ratio of 10% to separate AGN/ULXs and SSPs.

Comparison of the models with the data in Figure 7 shows that the demarcation proposed by R25 is reasonably accurate; the observed line ratios of AGN in all panels fall where expected. In the bottom-left panel, the dwarf AGN (C. E. Hood et al. 2017) fall cleanly in the AGN region, while they lie at the border of AGN and ULXs/AGN in the top-left panel. Interestingly, in the top-right panel of Figure 7, the shock models span the ULX/AGN and pure AGN regimes, but in the bottom-right, they fall cleanly in the AGN category. The line ratios for I Zw 18 are clearly well away from the AGN regime, and lie, as expected from Figure 4, in the region attributable to ULXs/AGN.

Overall, this comparison of the models with broad galaxy populations and I Zw 18 suggests that: (1) as stressed by R25, no single line ratio is a foolproof diagnostic of excitation mechanisms; (2) more than one physical mechanism, such as photoionization and shocks, can shape the properties of the ISM in galaxies, at least judging from our emission-line ratio analysis. Furthermore, for I Zw 18, comparison of the models with the observed line ratios clearly indicates that the high excitation of the gas, particularly in the NW, is compatible with the hard RF produced by low-metallicity ULXs. Nevertheless, the ambiguity with these and the IMBH contribution with light seeds and $f_{\rm AGN} = 0.04$, does not allow ruling out a small contribution from a low-mass IMBH (see also M. Mingozzi et al. 2025).

4. MIRI Continuum Sources

As described in Section 2.2, four sources, only one of which was previously known, were identified as compact continuum emitters by visual inspection of the MIRI spectral cubes. Here we describe their properties in terms of size and estimated age. Close-ups of these four objects from our MIRI imaging are shown in Figure 8, with F560W, F1130W, and F2550W from the top row to the penultimate; the bottom row gives a comparison with HST ACS/F606W. The spatial resolution of the images is shown as a hatched circle in the bottom-left corner of each panel corresponding to the FWHM of the PSF.[32] When Figure 8 is compared to Figure 1, it is easily appreciated that neither VLA-SE nor the central position of the SE star complex correspond to peaks in the continuum maps.

We estimated the sizes of the continuum sources in the MIRI images by examining radial profiles and comparing them with the profile of the PSF at that wavelength.[33] Figure 9 shows these profiles within concentric circular apertures centered on the positions in Table 1. The extraction of radial profiles and the photometry described below was performed using `Astropy/Photutils` (L. Bradley et al. 2024). We have estimated empirically the size of these sources in the three MIRI images by calculating the half-width at half-maximum (HWHM) from the profiles, and comparing it to the HWHM of the PSF. Because tests showed that results were more reliable with the oversampled PSF (×4 of the nominal pixel scale), we also extracted the profiles at the same oversampled pixel scale. The profiles have been normalized to have a maximum of unity; the vertical dotted line shows the HWHM corresponding to the 50% level, relative to this normalized maximum. The procedure was repeated in the same way for the PSF profiles; the PSF FWHMs determined from our procedures are, on average, 5% larger than those given in the JWST documentation.[34] This is a reasonable agreement, so that the application of our algorithms to both the

[32] The HST PSF has been taken from https://hst-docs.stsci.edu/acsihb/chapter-5-imaging/5-6-acs-point-spread-functions.

[33] We have adopted the MIRI imaging PSFs from https://stsci.app.box.com/v/jwst-simulated-psf-library/folder/174727061405. In our analysis, we use PSFs with the oversampling, ×4 the detector pixel scale.

[34] See https://jwst-docs.stsci.edu/jwst-mid-infrared-instrument/miri-performance/miri-point-spread-functions#gsc.tab=0.

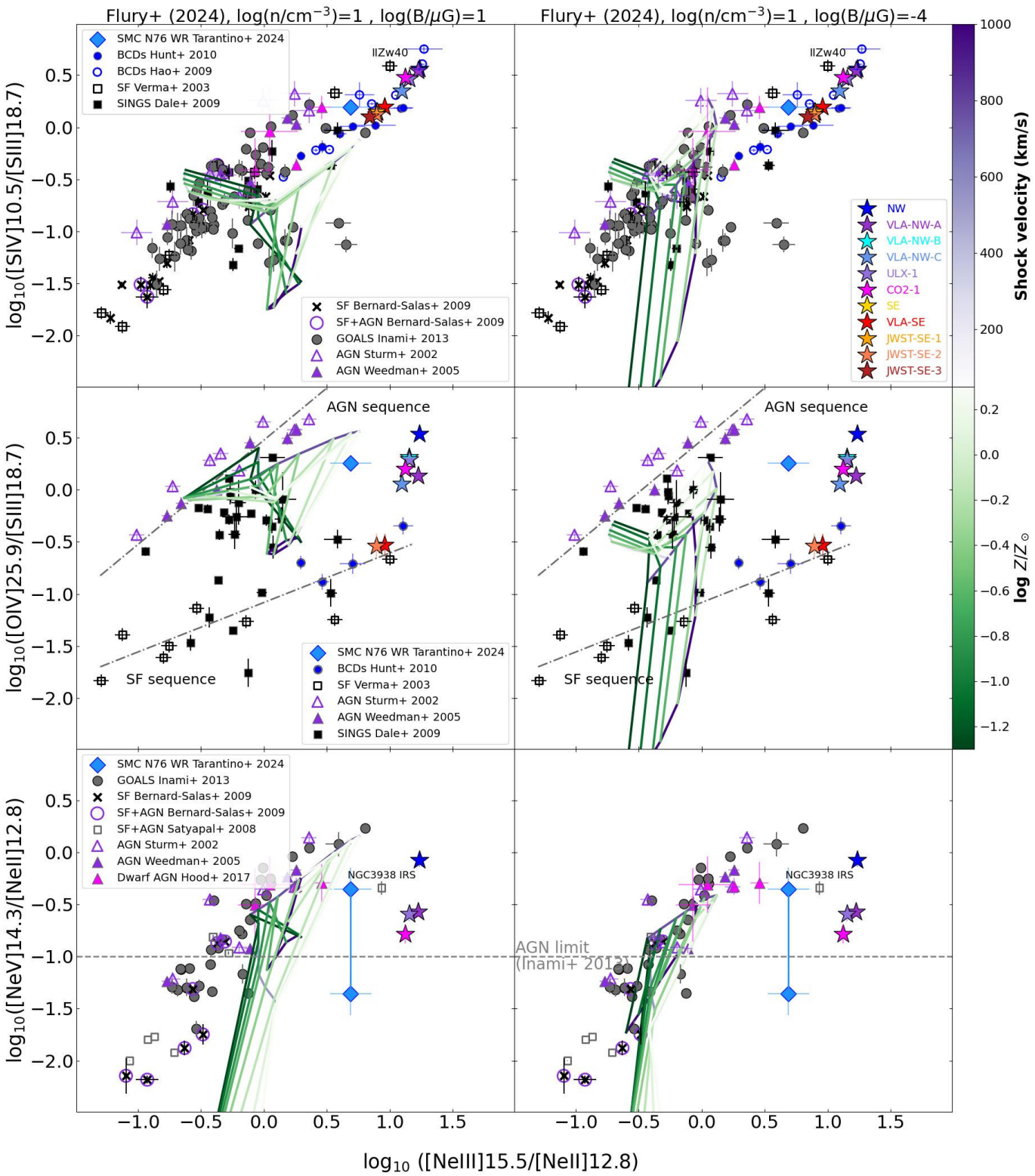

Figure 6. Line ratios are the same as in Figure 4, but here with the shock models from S. R. Flury et al. (2024) overlaid on the data points. As in Figure 4, when the error bars are not evident, they are smaller than the symbol. The color maps for the model grids for shock velocity and $\log(Z/Z_\odot)$ are the same for all panels. Two of the F24 models are shown, both of which having a pre-shock density of 10 cm^{-3}; the left panel gives the highest magnetic field B modeled by them, with 10 μG, and the right panel gives the lowest value, 10^{-4} μG. In the bottom panel, the horizontal dashed line corresponds to the AGN criterion of [Ne V]/[Ne II] $\geqslant 0.1$ defined by H. Inami et al. (2013).

PSF and source profiles should ensure consistent results. The intrinsic source sizes have been calculated by subtracting in quadrature the PSF FWHM from the source FWHM, taking the square root, then converting to parsecs. The results from our fits are reported in Table 4, where the uncertainties are given in parentheses in the following row.

Deconvolved source diameters (FWHM) of the continuum sources in I Zw 18 range from $\sim$20 pc to $\gtrsim$70 pc at F560W,

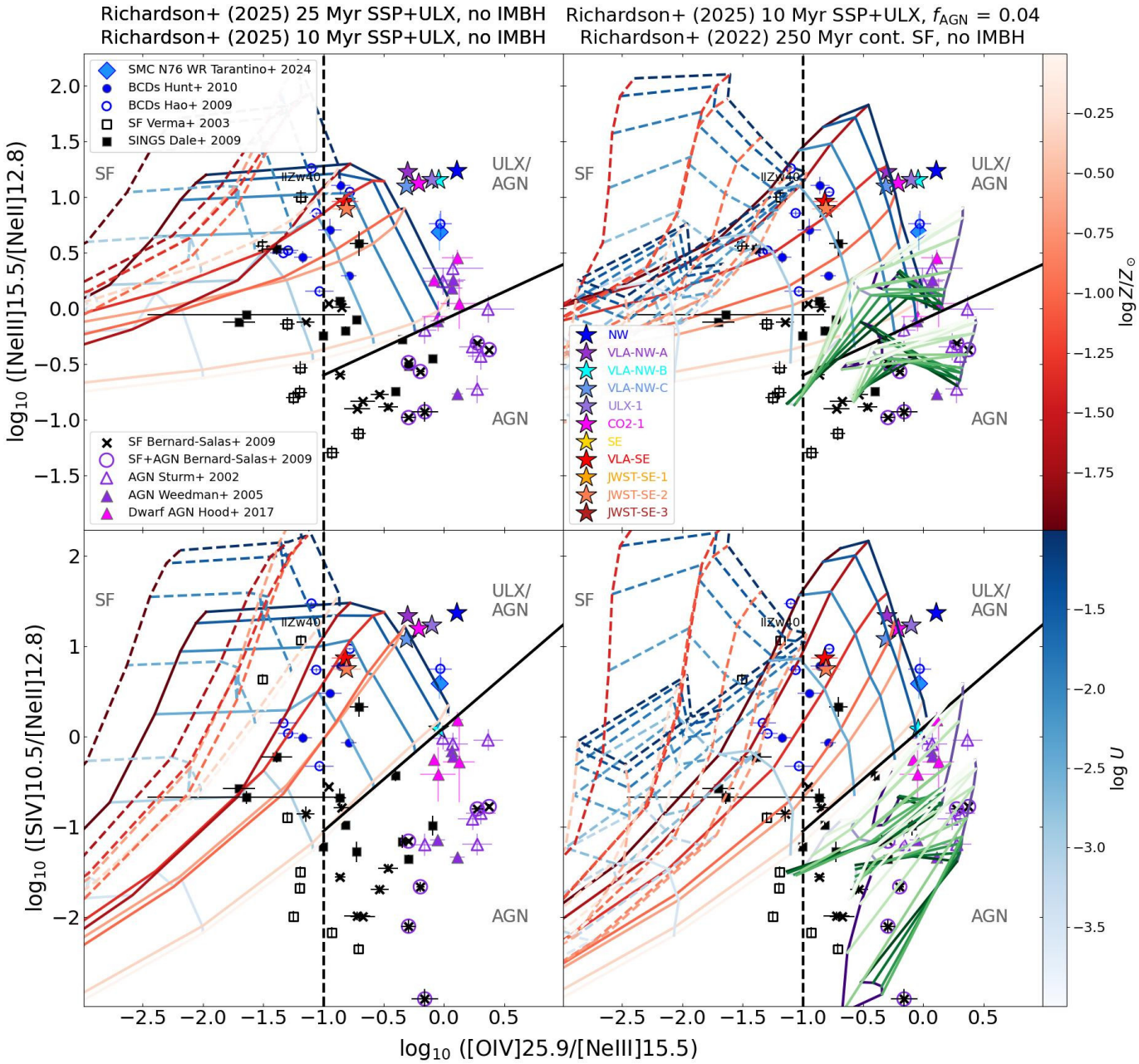

Figure 7. The observed line ratios considered to be the strongest diagnostics by R25. As in Figure 4, when the error bars are not evident, they are smaller than the symbol. The demarcation lines shown from Equations (9) and (10) in R25 separate stars+ULX excitation from that requiring an AGN, and also clearly delineate shocks from photoionization from stars. Left panel: the R25 models from Figure 4 are shown as in Figure 4, with the 25 (10) Myr SSP+ULX given as solid (dashed) curves. Right panel: the F24 shock models are shown as in Figure 6 (with the same color coding, not shown here). As in Figure 4, the R25 models with $f_{AGN} = 0.04$ are given as solid contours, while the R22 models are dashed ones.

and from ∼20 pc to ∼50 pc at F1130W; they are slightly larger at F2550W. JWST-SE-1 and JWST-SE-3 are only slightly resolved at F1130W, with deconvolved diameters ∼20 pc, but more resolved and slightly broader at F560W. The complexity of the region around JWST-SE-2 at F2550W enlarges its deconvolved size to $\gtrsim$100 pc, but, interestingly, at F1130W, its emission is more concentrated and slightly resolved. The deconvolved dimensions ∼50–70 pc of VLA-NW-A in all filters tend to be slightly larger (except for JWST-SE-2, F2550W) than the other three continuum sources.

To further investigate the nature of these continuum sources, we have compared photometry of the sources in the three MIRI filters with SED templates of star clusters as a function of age by B. C. Whitmore et al. (2025). Although such a comparison is not ideal, mainly because the templates are derived from NGC 628, a spiral galaxy with roughly solar metallicity, it can place the properties of the sources in I Zw 18 in a broader context. To this end, we performed aperture photometry from the MIRI images on each of the continuum sources, and compared it with the integrated flux from the profile; the total fluxes agree to within 10%. However, because the profiles extend to radii of $\gtrsim 2''$ (see Figure 8), we preferred to analyze the photometry within a circular aperture of radius $0''.65$, the same as the spectral extraction aperture. Local background in an annulus with a radius of $2''$ and width of $0''.2$ was subtracted before calculating the flux within the aperture.

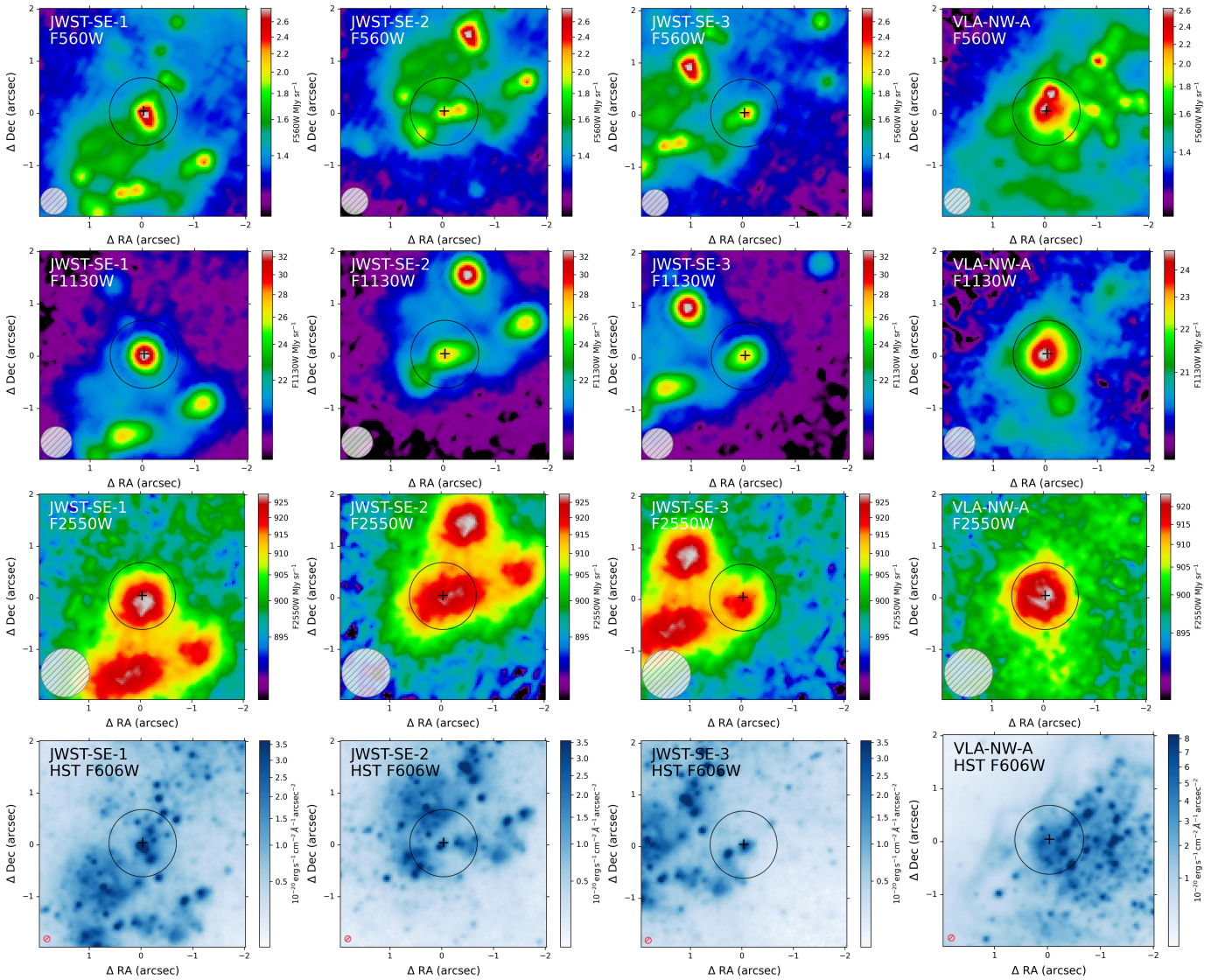

Figure 8. $4'' \times 4''$ cutouts of the MIRI 14 μm continuum sources: from left to right JWST-SE-1, JWST-SE-2, JWST-SE-3, and VLA-NW-A, and from top to bottom F560W, F1130W, F2550W, and HST/F606W. The images are centered on the respective 14 μm emission peaks (Table 1), shown by a +, and surrounded by the 0.″65-radius aperture used for spectroscopic extraction shown by a concentric circle. The FWHM of the PSF is shown as a hatched circle in the bottom-left corner of each panel.

Table 4 reports the photometry and the associated uncertainties. Although the small aperture used here suffers from losses at the longest wavelength (F2550W), it is a reasonable comparison with the B. C. Whitmore et al. (2025) templates, since they use small-aperture photometry for the derivation of the templates, with MIRI apertures corresponding to 50% encircled energy for point sources (radius of 0.″42 at F2100W; see M. J. Rodríguez et al. 2025). We have also checked the SED comparison with photometry for our continuum sources measured in larger apertures, and the age classification is the same.

Figure 10 shows this comparison, where the four I Zw 18 continuum sources are given as filled stars, and the SEDs have been normalized to our shortest-wavelength MIRI filter, F560W. Various ages from the templates[35] are shown by colored curves as reported in the legend. The templates do not extend to 25 μm, so the F2550W photometry can be viewed as an extrapolation (shown as dashed lines in Figure 10). When compared with the templates from B. C. Whitmore et al. (2025), the ages of the JWST-identified continuum sources appear to be quite young, $\lesssim$3–4 Myr. The radio-identified H II region VLA-NW-A seems slightly older, $\sim$5 Myr. Despite the silicate absorption feature at $\sim$10 μm and the prominent PAH feature at 7.7 μm in the templates, not seen in I Zw 18 (see Figure 2), all four I Zw 18 continuum sources would fall in the category of "nearly embedded cluster candidates" according to the SED templates provided by B. C. Whitmore et al. (2025).

These JWST continuum sources seem to be metal-poor YSCs. The low dust content and low extinction in I Zw 18 suggests that they cannot be partially embedded, like the YSCS in NGC 628 and other nearby galaxies. This is yet another limitation of the templates of B. C. Whitmore et al. (2025) when applied to I Zw 18. Indeed, the cluster candidates are clearly visible in the HST images (bottom panel of Figure 8). Typical young massive clusters have diameters of $\lesssim$10 pc as found in other nearby galaxies and starbursts such as

[35] Obtained from https://archive.stsci.edu/hlsp/phangs/phangs-cat.

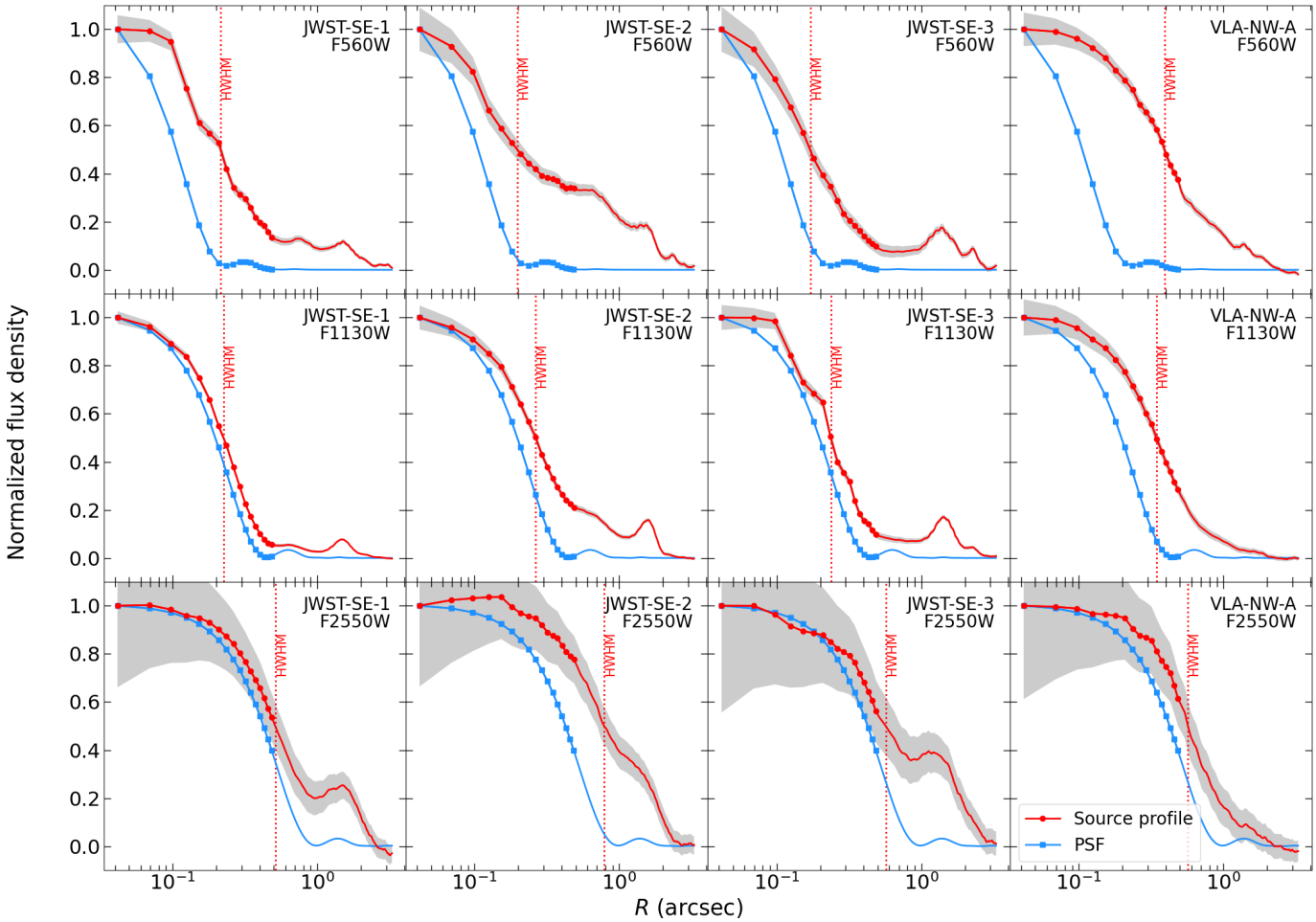

Figure 9. Radial profiles centered on the four continuum sources in the three MIRI imaging filters. The source profiles are shown as red curves, and the PSF is with blue curves, as shown in the legend in the bottom-right panel. The source profiles have been resampled to the same pixel scale as the PSFs, taken from the MIRI website; see the text for more details. All profiles are normalized to the peak amplitude, and individual radial sampling points are shown up to $R = 0\farcs5$. The HWHM of the source profile is given by a vertical dotted line. The gray shaded regions illustrate the 1σ uncertainties, calculated from the uncertainties in the source profile and the global background.

Table 4
Aperture Photometry and Sizes of Continuum Sources

Region	Flux[a] (mJy)			HWHM[b] (arcseconds)			Deconvolved FWHM[c]		
	F560W	F1130W	F2550W	F560W	F1130W	F2550W	F560W	F1130W	F2550W
JWST-SE-1	0.0101	0.0754	0.5615	0.215	0.225	0.512	0.″375 (33.1 pc)	0.″216 (19.1 pc)	0.″571 (50.3 pc)
	(0.0009)	(0.0023)	(0.0239)	(0.007)	(0.004)	(0.08)	…	…	…
JWST-SE-2	0.0103	0.0677	0.7229	0.198	0.265	0.786	0.″333 (29.4 pc)	0.″352 (31.1 pc)	1.″322 (116.6 pc)
	(0.0009)	(0.0022)	(0.0241)	(0.026)	(0.009)	(0.14)	…	…	…
JWST-SE-3	0.0048	0.0466	0.4528	0.171	0.237	0.568	0.″266 (23.5 pc)	0.″261 (23.0 pc)	0.″752 (66.4 pc)
	(0.0006)	(0.0019)	(0.0237)	(0.013)	(0.006)	(0.16)	…	…	…
VLA-NW-A	0.0163	0.0551	0.5461	0.392	0.344	0.569	0.″753 (66.5 pc)	0.″564 (49.8 pc)	0.″755 (66.7 pc)
	(0.0011)	(0.0020)	(0.0239)	(0.011)	(0.013)	(0.087)	…	…	…

Notes.
[a] Circular-aperture photometry with radii of 0.″65, with local background subtracted. The formal photometric uncertainties are given in the subsequent rows enclosed by parentheses. More details are given in the text.
[b] The uncertainties in the HWHM determinations are given in the subsequent rows enclosed by parentheses.
[c] Deconvolved FWHM are calculated by subtracting in quadrature the PSF FWHM, taking the square root, and converting to parsecs at the distance of I Zw 18, 18.2 Mpc. Measured HWHMs for the PSFs are 0.″2562, 0.″2962, and 0.″4712, for F560W, F1130W, and F2550W, respectively.

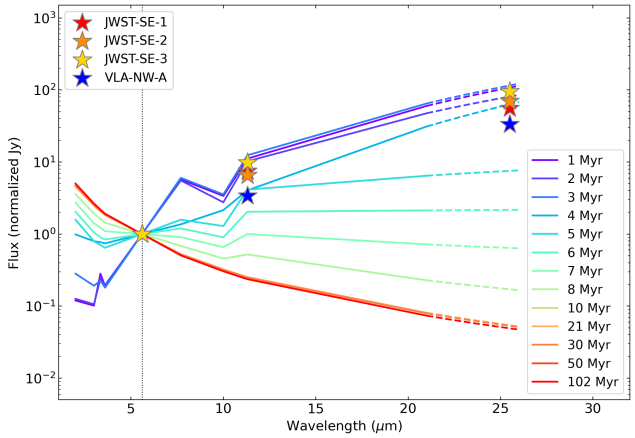

Figure 10. Comparison of MIRI imaging aperture photometry of the four continuum sources with photometric templates of star clusters as a function of age from B. C. Whitmore et al. (2025). All SEDs are normalized to 5.6 μm. The continuum sources are shown as filled stars, and the different ages of the templates correspond to the colors reported in the legend. The dashed lines are the extrapolation of the templates to the F2550W filter observed here.

M82, M83, NGC 253, NGC 3256, NGC 3351, NGC 4449, and NGC 5253 (e.g., A. K. Leroy et al. 2018; L. J. Smith et al. 2020; S. Deshmukh et al. 2024; R. C. Levy et al. 2024; S. T. Linden et al. 2024; T. McQuaid et al. 2024; J. Sun et al. 2024). Hence, we cannot be seeing the star clusters directly with MIRI, since the sizes of the MIRI sources are larger than this. Instead, with MIRI, we may be viewing the dust emission from the surrounding HII regions and neutral (partially molecular) clouds. In the Milky Way, emerging star clusters are very compact like those mentioned above, but the MIR emission is more extended since it comes from the surrounding cloud (e.g., E. Churchwell et al. 2006). Moreover, given the crowding and compact size of the sources in the HST image, the larger MIR sizes may also reflect the possibility that the continuum sources comprise more than one star cluster.

From a statistical perspective, we would expect to see at least a few YSCs in I Zw 18. With an average SFR $\sim$ 0.2–1 $M_\odot$ yr^{-1} over the last 10 Myr (L. K. Hunt et al. 2005; F. Annibali et al. 2013), I Zw 18 would have formed at least $\sim 2 \times 10^6\,M_\odot$ in that time. Assuming a conservative cluster formation rate of $\sim$10% (meaning that essentially 10% of the mass formed in the last 10 Myr should be in star clusters; M. R. Krumholz et al. 2019), we would expect statistically to detect around two YSCs with mass $> 10^4\,M_\odot$, and about 20 clusters between 10^3 and $10^4\,M_\odot$. This last estimate is based on a power-law cluster mass function with a power-law index of -2 (M. R. Krumholz et al. 2019). Thus, it is possible that the JWST continuum sources are YSCs, with masses between 10^3 and $10^5\,M_\odot$, identified by the dust continuum associated with the surrounding H II regions.

The JWST 14 μm continuum sources resemble the class of 21 μm compact ISM sources found by H. Hassani et al. (2023) in several nearby star-forming galaxies. 92% of the sources identified by H. Hassani et al. (2023) are spatially associated with H II regions and 74% are coincident with a stellar complex identified by HST. Less then 10% of them are completely embedded in dust with no visible counterpart. Those 21 μm-selected sources also have Hα or CO emission, implying that they are associated with HII regions or molecular clouds. In Paper II, the rotational H_2 transitions of I Zw 18 in aperture spectra are presented; most of the warm H_2 in I Zw 18 is found in the SE, where all five apertures in the SE have five or more significant detections in the rotational lines from $J_{\rm upper}$ from 3–10, while in the NW, only VLA-NW-A, shows a similar number of detections. The presence of warm H_2, presumably associated with molecular clouds, further corroborates that the continuum sources identified here are of a similar class to the sources found by H. Hassani et al. (2023).

The diameters of the JWST 14 μm continuum sources including VLA-NW-A are similar to those of the spatially resolved 24 μm-selected sources in M 33 by S. Sharma et al. (2011), and the HII regions in M 83 (L. Della Bruna et al. 2022). Moreover, as evident in the bottom panel of Figure 8, they are visible at 0.6 μm with HST, so cannot be enshrouded by dust. The extinction A_V measured within the JWST-SE apertures is not significantly greater than the foreground extinction (see Figure 3), another indication that they are not embedded in their natal dust cloud. Like the 21 μm compact sources identified by H. Hassani et al. (2023), these MIRI continuum sources behave like H II regions, emitting H I recombination lines, as well as various FS lines ([S III], [S IV], [Ne II], [Ne III], and [Ar III]) discussed in Section 3.2. The HST images show multiple sources, possibly associated with the YSCs exciting the H II regions.

5. The Ionization Sources in I Zw 18

In Section 3, we showed that eight of the eleven 120 pc diameter regions selected in I Zw 18 harbor [O IV] 25.89 emission with an IP to create the ion of 54.9 eV; four of the regions also emit [Ne V] 14.32 with an IP of 97.1 eV (see Figures 11 and 12 in Appendix B). The highest ionization gas is found in the NW, within the NW OB complex, the VLA-NW-A H II region, the CO(2–1) aperture, and also, possibly most importantly, around the site of the ULX. In the SE, one of the three continuum sources, together with VLA-SE, contains [O IV] emission, and none contain significant [Ne V]. The high ionization in the NW, relative to the SE, is seen not only in these highly ionized lines, but also in elevated [Ne III]/[Ne II] and [S IV]/[S III] ratios (see Figure 4). These ratios for I Zw 18 fall on the extreme end of the range of previous observations across a wide range of galaxy types.

These results pose the question of the physical process or processes exciting this gas. In the following, we assess the various theoretical models analyzed in Section 3.3, as well as the empirical comparison with SMC N76 WR, and other models for I Zw 18 in the literature.

5.1. Shocks

Fast radiative shocks have been frequently proposed as the mechanism powering the high-ionization lines in BCDs (e.g., T. X. Thuan & Y. I. Izotov 2005; Y. I. Izotov et al. 2012, 2021). However, we find that although they reproduce quite well some of the line ratios from known AGN, the F24 shock models are unable to reproduce the MIRI line ratios of I Zw 18. Other shock models such as A. Alarie & C. Morisset (2019), tested by M. Mingozzi et al. (2025), give similar results. Thus, we conclude that shocks could help regulate the line ratios of massive galaxies with or without AGN, but they are not responsible for the MIR high-ionization emission lines in I Zw 18.

5.2. IMBHs

As shown in Figures 4 and 7, even a small $f_{\rm AGN}$ of 4% can reproduce fairly well the line ratios observed in I Zw 18. Because of the similarity in ionizing SEDs (see Figure 5) and the modeled line ratios for the 25 Myr SSP+ULX populations and those including IMBH $f_{\rm AGN} = 0.04$, we cannot rule out a small IMBH in I Zw 18 on the basis of line ratios alone. Indeed, M. Mingozzi et al. (2025) found that a 4%–16% contribution from a $\sim 10^5\,M_\odot$ IMBH is needed to reproduce the strong [Ne V]/[Ne II] emission seen in SBS 0335−052, a BCD with $Z/Z_\odot \sim 5\%$. This will be further discussed in a forthcoming paper (R. J. Rickards Vaught et al. 2025, in preparation).

5.3. Feedback from Star Clusters

Shocked stellar winds from star clusters and supernovae can produce hot diffuse gas that emits X-rays (e.g., R. A. Chevalier & A. W. Clegg 1985; M. Cerviño et al. 2002). Such gas has been modeled extensively in the literature, but recent models focus on explaining the He II emission in dwarf galaxies via X-ray heating. Because of slower stellar winds at low metallicity, L. M. Oskinova & D. Schaerer (2022) found that plasma temperatures are lower, and the production rate of He II ionizing photons is higher. Thus, they argue that their model is consistent with the He II observed in I Zw 18 (e.g., C. Kehrig et al. 2021; R. J. Rickards Vaught et al. 2021).

Alternatively, the models by A. Franeck et al. (2022) use a different approach to estimate the soft X-ray emission of hot gas from star-cluster winds. The X-ray emission that would be observed in the scenario of hot diffuse gas produced by star clusters and supernovae is expected to be faint. Thus, it falls below the observed X-ray emission of the comparison sample of A. Franeck et al. (2022), and L. M. Oskinova & D. Schaerer (2022) argued that the diffuse hot gas in I Zw 18 is also too faint to be detected. Thus, with current observations, it is difficult to test this hypothesis, without radiative transfer models that predict line ratios under such conditions.

5.4. WR Stars

Because of the similarity of the line ratios observed in the SMC N76 WR nebula and I Zw 18, stars like AB7 (Y. Nazé et al. 2003; T. Shenar et al. 2016; E. Tarantino et al. 2024) could be responsible for ionizing the gas in I Zw 18. As mentioned above, I Zw 18 hosts WR stars found with long-slit spectroscopy (Y. I. Izotov et al. 1997; F. Legrand et al. 1997), and a WR blue bump has been identified in the NW by C. Kehrig et al. (2016). Moreover, the SED of WR N76 shown in Figure 5 from T. Shenar et al. (2016) is very similar below ∼100 eV to the R25 25 Myr 1% solar metallicity ionizing source, which comes close to reproducing the observed line ratios in I Zw 18.

Although WR stars in I Zw 18 have been previously dismissed as unable to power the highly ionized gas in I Zw 18 (C. Kehrig et al. 2015), the resemblance of the MIR high-ionization line ratios in I Zw 18 with SMC WR N76 suggests that one or a few stars like AB7 in I Zw 18 could be responsible. Such a mechanism would be particularly important in the SE where two apertures show [O IV] emission, relatively far away from ULX-1 in the NW. R. J. Rickards Vaught et al. (2021) also suggested that the He II emission seen in the SE could be powered by a single star like AB7.

It is probable that the YMCs in the MIRI-identified continuum sources host at least one WR star or WR binary such as AB7; C. Leitherer et al. (2014) predicted that at subsolar metallicity, the ratio between WR and O stars peaks at ∼5% between 3 and 4 Myr; with $\gtrsim$500 O stars in the SE alone, we would thus expect $\gtrsim$25 WR stars in the SE. The inferred young age of 3–4 Myr of the SE continuum sources from Figure 10 would be consistent with this, and with the ionizing sources comprising WR stars/binaries.

5.5. ULXs

The ULX in I Zw 18 is located in the NW, and the ULX-1 120 pc diameter aperture overlaps slightly with VLA-NW-A, CO2-1, and NW (see Figure 1). All six NW apertures show [O IV] 25.89 emission, and the four apertures near the ULX also show [Ne V] 14.32. The latest measurements of the 0.3–10 keV X-ray luminosity of ULX-1 in I Zw 18 give $L_{\rm X} \gtrsim 1.1 \times 10^{40}\,{\rm erg\,s^{-1}}$, suggesting a possible supercritical accretion state (P. Kaaret & H. Feng 2013; M. Yoshimoto et al. 2024). It is well known that ULXs are capable of generating large highly ionized nebulae a few hundreds of parsecs in diameter, observable both in the radio continuum (e.g., C. T. Berghea et al. 2020; R. Soria et al. 2021) and the optical (e.g., D.-S. Moon et al. 2011; P. Kaaret et al. 2017; A. Gúrpide et al. 2022). Such nebulae could be what we are observing in I Zw 18; indeed, V. Lebouteiller et al. (2017) attributed the heating source in the NW region of I Zw 18 to photoionization by radiation from a bright XRB.

The centers of VLA-NW-A and NW are at a projected distance of ∼150 pc from ULX-1, while CO2-1 is slightly closer in projection. If ULX-1 were to explain the He II, [O IV], and [Ne V] emission seen in those regions (for He II, see C. Kehrig et al. 2021; R. J. Rickards Vaught et al. 2021), the ULX would have to maintain a large He III region, with radius $R_{\rm He\,III} \approx 200$ pc, with He III recombining to He II at a rate

$$\dot{N}_{\rm He\,II} \approx \frac{4\pi}{3} R^3_{\rm He\,III}\, 0.08 n_e^2\, \alpha_{\rm He\,III} \approx 10^{49.9}\left(\frac{R_{\rm He\,III}}{200{\rm pc}}\right)^3\left(\frac{n_e}{{\rm cm^{-3}}}\right)^2\left(\frac{\alpha_{\rm He\,III}}{10^{-12}{\rm cm^3 s^{-1}}}\right){\rm s^{-1}}, \quad (1)$$

where $\alpha_{\rm He\,III}$ is the rate coefficient for radiative recombination He III → He II. If these recombinations are balanced by photoionizations, the required ULX luminosity is

$$L_{\rm X} \approx 100\,{\rm eV} \times \dot{N}_{\rm He\,III} \approx 10^{40.1}\left(\frac{R_{\rm He\,III}}{200{\rm pc}}\right)^3\left(\frac{n_e}{{\rm cm^{-3}}}\right)^2\left(\frac{\alpha_{\rm He\,III}}{10^{-12}{\rm cm^3 s^{-1}}}\right){\rm erg\,s^{-1}}. \quad (2)$$

Thus, if the rms electron density is $\sim 1\,{\rm cm^{-3}}$, the ULX in I Zw 18 could plausibly sustain the highly ionized gas, [Ne V] and [O IV] (and He II), seen in these NW apertures.

5.6. [Ne V] and AGN

[Ne V] is widely regarded as an indicator of an accreting massive BH (e.g., H. Inami et al. 2013; A. Feltre et al. 2016; J. Chisholm et al. 2024). Thus, if we were to take the [Ne V] detections in the four NW apertures at face value, we would conclude that there is an accreting massive BH or AGN in I Zw 18. However, the location of I Zw 18 in the line-ratio

diagnostics proposed by R25 shown in Figure 7 suggests that either a ∼25 Myr SSP+ULX or a ∼10 Myr SSP+ULX+AGN with a very small f_{AGN} of 4% could be responsible. The difference between a pure SSP+ULX, and one including a very small AGN fraction from IMBH emission, is not easy to distinguish only from line ratios. Given the similarity of the gas properties of I Zw 18 with high-z metal-poor dwarf galaxies, our observations furnish a cautionary tale for automatically associating highly ionized-gas detections such as [Ne V] with an AGN. The extreme low-metallicity environment in I Zw 18, more pronounced in the NW, can mimic the harsh RF environment surrounding an accreting massive BH.

6. Summary

In order to characterize the ISM in an extreme, metal-poor dwarf galaxy, we obtained MIRI/MRS observations of the main body of I Zw 18. We have selected 11 apertures, ∼120 pc in diameter, centered on regions of interest across the galaxy, and extracted 1D spectra within them (Figure 2). Our findings can be summarized as follows:

1. By comparing the MIRI H I recombination lines with the Hβ and Hδ lines from KCWI IFU maps of I Zw 18 (R. J. Rickards Vaught et al. 2021), we have verified the very low extinction of A_V ∼0.1–0.2 mag (Figure 3) previously found in the optical (e.g., Y. I. Izotov et al. 1999; C. Kehrig et al. 2015). Because of the small extinction in the MIR, it was not possible to perform the measurements using MIRI alone.
2. In addition to numerous HI recombination lines, we have detected a plethora of MIR fine-structure lines in I Zw 18, including [Ar II], [Ar III], [Fe II], [Ne II], [Ne III], [S III], and [S IV], as well as [P III] (weak detection in only one aperture; see Table 2). Also detected are extremely high-ionization emission lines including [O IV] 25.89 with an IP of 54.9 eV and [Ne V] 14.32 (IP = 97.1 eV). [Ne V] 14.32 has never been detected in a dwarf galaxy before JWST (see M. Mingozzi et al. 2025, for the detection of [Ne V] 14.32 in SBS 0335−052).
3. The line ratios of the lower ionization lines in I Zw 18 ([Ne II], [Ne III], [S III], [S IV]) are consistent, at the extreme end, with previous observations of BCDs and other galaxies. However, the higher ionization lines ([O IV], [Ne V]), found mainly in the NW, fall in regions of the line-ratio diagrams that do not coincide with massive star-forming galaxies or known AGN. Comparison with state-of-the-art photoionization and shock models shows that the line ratios in I Zw 18 cannot be well reproduced by shocks. However, they are fairly well approximated with low-metallicity stellar populations containing a self-consistent substantial ULX component. Wolf–Rayet stars like AB7 in the SMC or a small 4% contribution from an IMBH could also be responsible (see Figures 4, 6, and 7). Ultimately, the confluence of more than one of the physical processes discussed here could be powering the ionization state of I Zw 18.
4. From the MIRI cube, we identified four JWST/MIRI continuum sources at 14 μm, one of which is associated with the radio HII region VLA-NW-A, and three of which were not previously characterized (see Figure 8). Their deconvolved diameters of ∼30–100 pc are larger than the ∼10 pc diameter of typical young massive star clusters, and they have apparently emerged from their natal dust cloud because of the low measured extinction, and the existence of an HST counterpart at F606W. Comparison of the SEDs with templates of YSCs by B. C. Whitmore et al. (2025) suggests that they are associated with YSCs, and that we are seeing the dust continuum from the surrounding H II regions and neutral (partially molecular) clouds. Such objects would be expected statistically, given the cluster nature of SF. Their sizes are consistent with 21−24 μm-selected sources in M33 and in other nearby galaxies (S. Sharma et al. 2011; H. Hassani et al. 2023).

It is becoming increasingly evident that JWST/MIRI is a uniquely powerful facility for characterizing the ISM in nearby galaxies, even in faint, extremely metal-poor dwarfs such as I Zw 18. The extreme conditions in the ISM of I Zw 18 can serve as a local benchmark to compare to the metal-poor dwarf-galaxy population now being identified by JWST at high redshift.

Acknowledgments

We thank the referee for providing a timely and insightful report, and for the attentive comments that helped improve the paper. We are also grateful to Tomer Shenar, who kindly made available the SED of AB7 in the SMC (T. Shenar et al. 2016). This work is based on observations made with the NASA/ESA/CSA James Webb Space Telescope. The data were obtained from the Mikulski Archive for Space Telescopes at the Space Telescope Science Institute, which is operated by the Association of Universities for Research in Astronomy, Inc., under NASA contract NAS 5-03127 for JWST. These observations are associated with program JWST-3533. R.R.V. is grateful for the support of this program, provided by NASA through a grant from the Space Telescope Science Institute. A.B.-Z. acknowledges support by NASA under award No. 80GSFC24M0006. B.L.J. and M. Mingozzi are thankful for support from the European Space Agency (ESA). M. Meixner acknowledges that a portion of her research was carried out at the Jet Propulsion Laboratory, California Institute of Technology, under a contract with the National Aeronautics and Space Administration (80NM0018D0004). L.K.H. thanks Martha Haynes for very interesting discussions, and for sharing her physical insight into low-metallicity galaxies in general, and I Zw 18 in particular. This research made use of `Photutils`, an `Astropy` package for detection and photometry of astronomical sources (L. Bradley et al. 2024).

Facilities: JWST (MIRI), HST (ACS), Keck (KCWI).

Software: Astropy (Astropy Collaboration et al. 2013, 2018), Numpy (C. R. Harris et al. 2020), SciPy (P. Virtanen et al. 2020), Dustmaps (G. Green 2018).

The JWST data presented in this article were obtained from the Mikulski Archive for Space Telescopes (MAST) at the Space Telescope Science Institute. The specific observations analyzed can be accessed via doi: 10.17909/n80x-b534.

Appendix A
Detailed Description of MRS Data Reduction

Background subtraction was performed separately from the pipeline at the exposure level, using the rate files after the

calwebb_detector1 step. A master background was created from the background observation rate files for each detector and subtracted accordingly. The presence of warm pixels in the final products was mitigated using LaCosmic, a well-known Python package for cosmic-ray removal based on P. G. van Dokkum (2001). LaCosmic was applied to the rate files with a contrast setting of 2 and a cosmic-ray threshold (cr_threshold) of 25. The neighbor_threshold was set to 5, which effectively flagged cosmic rays that had not been detected in earlier pipeline steps. Additionally, a warm pixel mask was created for each detector and added to the DQ extension of the calibrated files after the calwebb_spec2 step.

The calwebb_spec2 step was executed with the residual_fringe correction enabled. This step addresses residual fringes that may persist after the initial fringe flat correction. Even small variations in the position observed can result in significantly different fringe patterns. The residual_fringe step models these residual fringes as a summation of sinusoidal components. Additional fringe corrections were applied to the final extracted spectra. At this stage, the warm pixel mask was incorporated into the DQ extension of the calibration files before the cube-building process. The astrometric and distortion corrections were also applied in this step according to P. Patapis et al. (2024).

Finally, the calwebb_spec3 step was executed. During the outlier_detection step, any remaining unflagged warm pixels were identified by setting threshold_percent to 99.8, and kernel_size to [11,11]. In the cube_build step, the output_type was set to band, allowing a third fringe correction to be applied on a band-by-band basis.

Appendix B
Flux Measurements of Detected Lines and Gaussian Fits for Detected [O IV] and [Ne V]

Figures 11 and 12 show the fits for the high-ionization lines O IV and Ne V, and Tables 5 and 6 report the measured fluxes within a radius of 0.″65 as described in Section 2.2.

Table 5
Integrated Line Fluxes in the NW-region Apertures with S/N ⩾ 3

Line	Rest λ (μm)	NW	VLA-NW-A	VLA-NW-B	VLA-NW-C	CO2-1	ULX-1
			(10^{-21} W m^{-2})				
H I Recombination Lines							
H I (10–6)	5.1287	⋯	25.93 ± 2.80	⋯	⋯	⋯	⋯
H I (10–7)	8.7601	6.36 ± 0.85	16.64 ± 0.97	⋯	8.01 ± 1.40	10.33 ± 1.10	8.49 ± 1.09
H I (10–8)	16.2091	4.01 ± 0.83	10.64 ± 0.66	⋯	5.69 ± 0.62	5.37 ± 0.63	3.67 ± 0.82
H I (12–9)	16.8806	1.70 ± 0.56	4.47 ± 0.58	⋯	2.31 ± 0.56	1.87 ± 0.57	⋯
H I (13–8)	9.392	10.14 ± 2.59	6.12 ± 0.93	⋯	7.94 ± 2.22	4.66 ± 1.22	4.48 ± 1.25
H I (13–9)	14.1831	⋯	3.27 ± 0.77	⋯	⋯	⋯	⋯
H I (15–9)	11.5395	⋯	2.50 ± 0.71	⋯	⋯	⋯	⋯
H I (17–7)	5.3798	⋯	18.95 ± 4.84	⋯	⋯	⋯	⋯
Pfα	7.4599	60.27 ± 1.68	183.10 ± 3.23	⋯	⋯	89.33 ± 2.39	68.54 ± 2.09
Huα	12.3719	23.95 ± 1.61	65.59 ± 3.89	14.10 ± 1.29	31.28 ± 2.61	32.51 ± 2.21	26.85 ± 1.76
Huβ	7.5025	16.31 ± 1.50	52.20 ± 3.67	⋯	8.58 ± 1.01	25.12 ± 2.04	19.26 ± 1.83
H I (8–7)	19.0619	⋯	25.69 ± 2.86	⋯	⋯	14.94 ± 2.08	⋯
Huγ	5.9082	9.15 ± 2.75	29.30 ± 4.29	⋯	⋯	⋯	⋯
H I (9–7)	11.3087	7.38 ± 0.74	22.73 ± 1.39	⋯	9.88 ± 0.90	12.10 ± 1.20	10.06 ± 1.05
Fine-structure Lines							
[Ar III]	8.9914	16.75 ± 1.02	54.64 ± 1.38	⋯	30.42 ± 1.11	30.72 ± 1.31	22.27 ± 0.81
[Fe II]	5.3402	11.56 ± 3.38	32.28 ± 5.76	⋯	⋯	19.85 ± 4.81	16.62 ± 4.67
[Ne III]	15.5551	177.30 ± 0.88	495.50 ± 2.21	111.50 ± 0.98	250.30 ± 1.45	280.60 ± 2.24	208.40 ± 1.62
[Ne II]	12.8135	10.26 ± 1.08	29.34 ± 0.51	7.79 ± 1.01	20.01 ± 0.89	21.06 ± 1.02	14.52 ± 0.98
[Ne V]	14.3217	8.60 ± 0.82	7.84 ± 0.77	⋯	⋯	3.44 ± 0.65	3.70 ± 0.53
[O IV]	25.8903	227.60 ± 8.65	247.80 ± 12.21	101.10 ± 7.33	122.60 ± 8.58	173.60 ± 11.61	165.60 ± 9.96
[P III]	17.885	⋯	2.72 ± 0.79	⋯	⋯	⋯	⋯
[S III]	18.713	66.60 ± 2.27	182.80 ± 3.16	49.55 ± 1.85	108.20 ± 2.74	110.10 ± 2.38	85.19 ± 2.51
[S IV]	10.5105	240.50 ± 2.72	637.20 ± 9.28	9.36 ± 1.23	241.00 ± 2.77	330.30 ± 3.95	247.80 ± 2.90

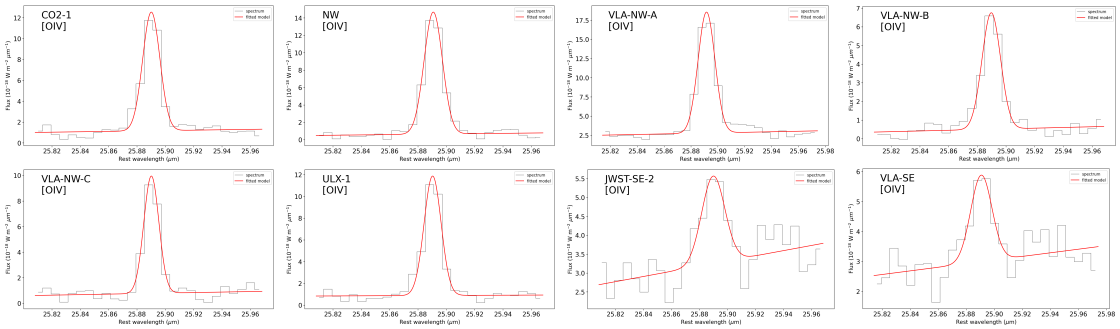

Figure 11. Gaussian line fits to the detected [O IV]; the vertical flux density scale is in units of 10^{-18} W m $^{-2}$ μm.

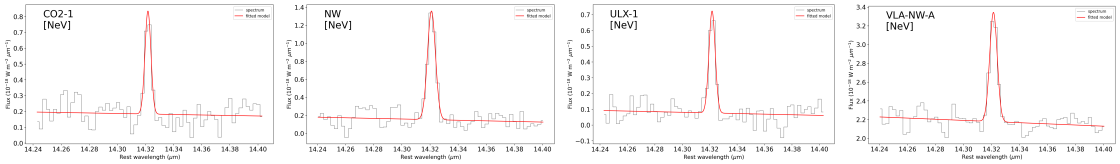

Figure 12. Gaussian line fits to the detected [Ne V]; the vertical flux density scale is in units of 10^{-18} W m $^{-2}$ μm.

Table 6
Integrated Line Fluxes in the SE-region Apertures with S/N $\geqslant$ 3

Line	Rest λ (μm)	JWST-SE-1	JWST-SE-2	JWST-SE-3 (10^{-21} W m^{-2})	SE	VLA-SE
			H I Recombination Lines			
H I (10–6)	5.1287	11.84 ± 3.39	13.32 ± 3.12	⋯	11.62 ± 2.81	15.20 ± 2.94
H I (10–7)	8.7601	9.23 ± 0.94	12.12 ± 1.30	7.13 ± 1.24	11.56 ± 1.18	13.43 ± 1.30
H I (10–8)	16.2091	5.37 ± 0.63	7.25 ± 0.78	2.76 ± 0.55	6.23 ± 0.59	8.04 ± 0.68
H I (12–9)	16.8806	⋯	2.46 ± 0.61	⋯	2.01 ± 0.57	2.62 ± 0.60
H I (13–8)	9.392	⋯	⋯	⋯	4.67 ± 1.10	⋯
H I (13–9)	14.1831	⋯	2.57 ± 0.77	⋯	⋯	2.81 ± 0.75
H I (14–7)	5.9568	⋯	10.20 ± 2.42	⋯	⋯	11.35 ± 2.40
HI(15-9)	11.5395	⋯	⋯	⋯	2.39 ± 0.46	2.42 ± 0.50
Pf α	7.4599	92.87 ± 2.26	117.90 ± 2.40	59.04 ± 2.14	104.50 ± 2.38	128.30 ± 2.51
Hu α	12.3719	32.64 ± 1.78	42.21 ± 2.58	18.04 ± 1.42	37.20 ± 2.10	48.26 ± 2.97
Hu β	7.5025	24.70 ± 2.02	30.99 ± 2.73	11.25 ± 1.78	26.17 ± 2.40	34.78 ± 3.15
HI(8-7)	19.0619	⋯	19.27 ± 2.01	⋯	13.72 ± 2.39	18.69 ± 2.08
Hu γ	5.9082	14.18 ± 3.12	18.44 ± 3.23	10.95 ± 2.10	16.43 ± 2.43	20.25 ± 3.12
H I (9–7)	11.3087	13.66 ± 0.94	15.55 ± 1.19	5.87 ± 0.88	13.66 ± 1.01	17.04 ± 1.03
			Fine-structure lines			
[Ar III]	8.9914	41.10 ± 1.01	45.68 ± 1.88	21.82 ± 1.16	44.22 ± 1.25	52.16 ± 1.63
[Ar II]	6.9853	12.66 ± 2.13	10.94 ± 1.62	⋯	12.78 ± 1.65	11.51 ± 1.44
[Fe II]	5.3402	36.34 ± 3.25	42.98 ± 6.41	21.94 ± 3.02	40.13 ± 3.06	44.79 ± 3.94
[Ne III]	15.5551	270.90 ± 1.95	308.20 ± 1.46	146.00 ± 0.81	292.00 ± 1.68	361.40 ± 1.66
[Ne II]	12.8135	34.16 ± 0.79	39.16 ± 0.92	20.98 ± 0.90	36.53 ± 0.88	39.56 ± 0.98
[O IV]	25.8903	⋯	47.94 ± 12.93	⋯	⋯	54.93 ± 13.93
[S III]	18.713	132.20 ± 1.95	166.70 ± 4.52	67.44 ± 2.78	143.20 ± 2.57	186.90 ± 3.91
[S IV]	10.5105	185.00 ± 2.42	219.60 ± 3.46	84.73 ± 1.27	198.60 ± 2.72	291.70 ± 3.84

ORCID iDs

L. K. Hunt https://orcid.org/0000-0001-9162-2371
A. Aloisi https://orcid.org/0000-0003-4137-882X
M. G. Navarro https://orcid.org/0000-0002-1860-2304
R. J. Rickards Vaught https://orcid.org/0000-0001-9719-4080
B. T. Draine https://orcid.org/0000-0002-0846-936X
A. Adamo https://orcid.org/0000-0002-8192-8091
F. Annibali https://orcid.org/0000-0003-3758-4516
D. Calzetti https://orcid.org/0000-0002-5189-8004
S. Hernandez https://orcid.org/0000-0003-4857-8699
B. L. James https://orcid.org/0000-0003-4372-2006
M. Mingozzi https://orcid.org/0000-0003-2589-762X
R. Schneider https://orcid.org/0000-0001-9317-2888
M. Tosi https://orcid.org/0000-0002-0986-4759
B. Brandl https://orcid.org/0000-0001-9737-169X

M. G. del Valle-Espinosa https://orcid.org/0000-0002-0191-4897
F. Donnan https://orcid.org/0000-0002-6460-3682
A. S. Hirschauer https://orcid.org/0000-0002-2954-8622
M. Meixner https://orcid.org/0000-0002-0522-3743
D. Rigopoulou https://orcid.org/0000-0001-6854-7545
C. T. Richardson https://orcid.org/0000-0002-3703-0719
J. M. Levanti https://orcid.org/0009-0003-6156-8310
A. R. Basu-Zych https://orcid.org/0000-0001-8525-4920

References

Alarie, A., & Morisset, C. 2019, RMxAA, 55, 377
Aloisi, A., Clementini, G., Tosi, M., et al. 2007, ApJL, 667, L151
Annibali, F., Cignoni, M., Tosi, M., et al. 2013, AJ, 146, 144
Argyriou, I., Glasse, A., Law, D. R., et al. 2023, A&A, 675, A111
Astropy Collaboration, Price-Whelan, A. M., Sipőcz, B. M., et al. 2018, AJ, 156, 123
Astropy Collaboration, Robitaille, T. P., Tollerud, E. J., et al. 2013, A&A, 558, A33
Atek, H., Furtak, L. J., Oesch, P., et al. 2022, MNRAS, 511, 4464
Atek, H., Labbé, I., Furtak, L. J., et al. 2024, Natur, 626, 975
Babul, A., & Ferguson, H. C. 1996, ApJ, 458, 100
Behroozi, P., Conroy, C., Wechsler, R. H., et al. 2020, MNRAS, 499, 5702
Behroozi, P., Wechsler, R. H., Hearin, A. P., & Conroy, C. 2019, MNRAS, 488, 3143
Berghea, C. T., Johnson, M. C., Secrest, N. J., et al. 2020, ApJ, 896, 117
Bernard-Salas, J., Spoon, H. W. W., Charmandaris, V., et al. 2009, ApJS, 184, 230
Bhowmick, A. K., Blecha, L., Torrey, P., et al. 2024, MNRAS, 531, 4311
Binette, L., Dopita, M. A., & Tuohy, I. R. 1985, ApJ, 297, 476
Bolatto, A. D., Wolfire, M., & Leroy, A. K. 2013, ARA&A, 51, 207
Bortolini, G., Östlin, G., Habel, N., et al. 2024, A&A, 689, A146
Bradley, L., Sipőcz, B., Robitaille, T., et al. 2024, astropy/photutils: v2.0.2, doi:10.5281/zenodo.13989456
Bromm, V., & Yoshida, N. 2011, ARA&A, 49, 373
Brown, T. M., Heap, S. R., Hubeny, I., Lanz, T., & Lindler, D. 2002, ApJL, 579, L75
Bullock, J. S., & Boylan-Kolchin, M. 2017, ARA&A, 55, 343
Bushouse, H., Eisenhamer, J., Dencheva, N., et al. 2024, JWST Calibration Pipeline, v1.15.0, doi:10.5281/zenodo.12556702
Calzetti, D., Kinney, A. L., & Storchi-Bergmann, T. 1994, ApJ, 429, 582
Campbell, A., Terlevich, R., & Melnick, J. 1986, MNRAS, 223, 811
Cannon, J. M., Skillman, E. D., Garnett, D. R., & Dufour, R. J. 2002, ApJ, 565, 931
Cannon, J. M., Walter, F., Skillman, E. D., & van Zee, L. 2005, ApJL, 621, L21
Carnall, A. C., Begley, R., McLeod, D. J., et al. 2023, MNRAS, 518, L45
Cerviño, M., Mas-Hesse, J. M., & Kunth, D. 2002, A&A, 392, 19
Chevalier, R. A., & Clegg, A. W. 1985, Natur, 317, 44
Chisholm, J., Berg, D. A., Endsley, R., et al. 2024, MNRAS, 534, 2633
Churchwell, E., Povich, M. S., Allen, D., et al. 2006, ApJ, 649, 759
Conselice, C. J., Adams, N., Harvey, T., et al. 2025, ApJ, 983, 30
Cormier, D., Madden, S. C., Lebouteiller, V., et al. 2015, A&A, 578, A53
Curti, M., D'Eugenio, F., Carniani, S., et al. 2023, MNRAS, 518, 425
Curti, M., Maiolino, R., Curtis-Lake, E., et al. 2024, A&A, 684, A75
Dale, D. A., Smith, J. D. T., Schlawin, E. A., et al. 2009, ApJ, 693, 1821
Davidzon, I., Ilbert, O., Laigle, C., et al. 2017, A&A, 605, A70
Decleir, M., Gordon, K. D., Andrews, J. E., et al. 2022, ApJ, 930, 15
Della Bruna, L., Adamo, A., McLeod, A. F., et al. 2022, A&A, 666, A29
Deshmukh, S., Linden, S. T., Calzetti, D., et al. 2024, ApJL, 974, L24
Draine, B. T. 2011, Physics of the Interstellar and Intergalactic Medium (Princeton, NJ: Princeton Univ. Press)
Draine, B. T., & Bertoldi, F. 1996, ApJ, 468, 269
Draine, B. T., & McKee, C. F. 1993, ARA&A, 31, 373
Earl, N., Tollerud, E., Jones, C., et al. 2020, astropy/specutils: v1.0, doi:10.5281/zenodo.3718589
Eldridge, J. J., Stanway, E. R., Xiao, L., et al. 2017, PASA, 34, e058
Endsley, R., Stark, D. P., Whitler, L., et al. 2024, MNRAS, 533, 1111
Engelbracht, C. W., Gordon, K. D., Rieke, G. H., et al. 2005, ApJL, 628, L29
Feltre, A., Charlot, S., & Gutkin, J. 2016, MNRAS, 456, 3354
Fisher, D. B., Bolatto, A. D., Herrera-Camus, R., et al. 2014, Natur, 505, 186
Fitzpatrick, E. L., Massa, D., Gordon, K. D., Bohlin, R., & Clayton, G. C. 2019, ApJ, 886, 108
Flury, S. R., Arellano-Córdova, K. Z., Moran, E. C., & Einsig, A. 2024, arXiv:2412.06763
Franeck, A., Wünsch, R., Martínez-González, S., et al. 2022, ApJ, 927, 212
Fumagalli, M., Krumholz, M. R., & Hunt, L. K. 2010, ApJ, 722, 919
Furtak, L. J., Shuntov, M., Atek, H., et al. 2023, MNRAS, 519, 3064
Gaia Collaboration, Brown, A. G. A., Vallenari, A., et al. 2021, A&A, 649, A1
Galliano, F., Nersesian, A., Bianchi, S., et al. 2021, A&A, 649, A18
Garofali, K., Basu-Zych, A. R., Johnson, B. D., et al. 2024, ApJ, 960, 13
Gil de Paz, A., Madore, B. F., & Pevunova, O. 2003, ApJS, 147, 29
Gordon, K. 2024, JOSS, 9, 7023
Gordon, K. D., Cartledge, S., & Clayton, G. C. 2009, ApJ, 705, 1320
Gordon, K. D., Clayton, G. C., Decleir, M., et al. 2023, ApJ, 950, 86
Gordon, K. D., Misselt, K. A., Bouwman, J., et al. 2021, ApJ, 916, 33
Green, G. 2018, JOSS, 3, 695
Gúrpide, A., Parra, M., Godet, O., Contini, T., & Olive, J. F. 2022, A&A, 666, A100
Hao, L., Wu, Y., Charmandaris, V., et al. 2009, ApJ, 704, 1159
Harris, C. R., Millman, K. J., van der Walt, S. J., et al. 2020, Natur, 585, 357
Hassani, H., Rosolowsky, E., Leroy, A. K., et al. 2023, ApJL, 944, L21
Heintz, K. E., Giménez-Arteaga, C., Fujimoto, S., et al. 2023, ApJL, 944, L30
Hernandez, S., Smith, L. J., Jones, L. H., et al. 2025, ApJ, 983, 154
Hirschauer, A. S., Crouzet, N., Habel, N., et al. 2024, AJ, 168, 23
Hood, C. E., Barth, A. J., Ho, L. C., & Greene, J. E. 2017, ApJ, 838, 26
Hunt, L. K., Draine, B. T., Navarro, M. G., et al. 2025, arXiv:2509.02690
Hunt, L. K., Dyer, K. K., & Thuan, T. X. 2005, A&A, 436, 837
Hunt, L. K., Testi, L., Casasola, V., et al. 2014, A&A, 561, A49
Hunt, L. K., Thuan, T. X., Izotov, Y. I., & Sauvage, M. 2010, ApJ, 712, 164
Hunt, L. K., Vanzi, L., & Thuan, T. X. 2001, A&A, 377, 66
Hunter, D. A., Jr., & Thronson, H. A. 1995, ApJ, 452, 238
Inami, H., Armus, L., Charmandaris, V., et al. 2013, ApJ, 777, 156
Izotov, Y. I., Chaffee, F. H., Foltz, C. B., et al. 1999, ApJ, 527, 757
Izotov, Y. I., Foltz, C. B., Green, R. F., Guseva, N. G., & Thuan, T. X. 1997, ApJL, 487, L37
Izotov, Y. I., & Thuan, T. X. 2016, MNRAS, 457, 64
Izotov, Y. I., Thuan, T. X., & Guseva, N. G. 2021, MNRAS, 508, 2556
Izotov, Y. I., Thuan, T. X., & Privon, G. 2012, MNRAS, 427, 1229
Janowiecki, S., Salzer, J. J., van Zee, L., Rosenberg, J. L., & Skillman, E. 2017, ApJ, 836, 128
Kaaret, P., & Feng, H. 2013, ApJ, 770, 20
Kaaret, P., Feng, H., & Roberts, T. P. 2017, ARA&A, 55, 303
Kehrig, C., Guerrero, M. A., Vílchez, J. M., & Ramos-Larios, G. 2021, ApJL, 908, L54
Kehrig, C., Vílchez, J. M., Pérez-Montero, E., et al. 2015, ApJL, 801, L28
Kehrig, C., Vílchez, J. M., Pérez-Montero, E., et al. 2016, MNRAS, 459, 2992
Klessen, R. S., & Glover, S. C. O. 2023, ARA&A, 61, 65
Krumholz, M. R., McKee, C. F., & Bland-Hawthorn, J. 2019, ARA&A, 57, 227
Law, D. R., E. Morrison, J., Argyriou, I., et al. 2023, AJ, 166, 45
Lebouteiller, V., Heap, S., Hubeny, I., & Kunth, D. 2013, A&A, 553, A16
Lebouteiller, V., Péquignot, D., Cormier, D., et al. 2017, A&A, 602, A45
Legrand, F., Kunth, D., Roy, J. R., Mas-Hesse, J. M., & Walsh, J. R. 1997, A&A, 326, L17
Leitherer, C., Ekström, S., Meynet, G., et al. 2014, ApJS, 212, 14
Lelli, F., Verheijen, M., Fraternali, F., & Sancisi, R. 2012, A&A, 537, A72
Leroy, A. K., Bolatto, A. D., Ostriker, E. C., et al. 2018, ApJ, 869, 126
Leslie, S. K., Schinnerer, E., Liu, D., et al. 2020, ApJ, 899, 58
Levy, R. C., Bolatto, A. D., Mayya, D., et al. 2024, ApJL, 973, L55
Linden, S. T., Lai, T., Evans, A. S., et al. 2024, ApJL, 974, L27
Looser, T. J., D'Eugenio, F., Maiolino, R., et al. 2025, A&A, 697, A88
Luridiana, V., Morisset, C., & Shaw, R. A. 2015, A&A, 573, A42
Madden, S. C., Galliano, F., Jones, A. P., & Sauvage, M. 2006, A&A, 446, 877
Madden, S. C., Rémy-Ruyer, A., Galametz, M., et al. 2014, PASP, 126, 1079
Martin, C. L. 1996, ApJ, 465, 680
McQuaid, T., Calzetti, D., Linden, S. T., et al. 2024, ApJ, 967, 102
Mingozzi, M., Garcia del Valle-Espinosa, M., James, B. L., et al. 2025, ApJ, 985, 253
Moon, D.-S., Harrison, F. A., Cenko, S. B., & Shariff, J. A. 2011, ApJL, 731, L32
Morishita, T., Stiavelli, M., Grillo, C., et al. 2024, ApJ, 971, 43
Nakajima, K., Ouchi, M., Isobe, Y., et al. 2023, ApJS, 269, 33
Nanni, A., Burgarella, D., Theulé, P., Côté, B., & Hirashita, H. 2020, A&A, 641, A168
Nazé, Y., Rauw, G., Manfroid, J., Chu, Y. H., & Vreux, J. M. 2003, A&A, 408, 171
Noeske, K. G., Weiner, B. J., Faber, S. M., et al. 2007, ApJL, 660, L43

Oskinova, L. M., & Schaerer, D. 2022, A&A, 661, A67
Ott, J., Walter, F., & Brinks, E. 2005, MNRAS, 358, 1423
Patapis, P., Argyriou, I., Law, D. R., et al. 2024, A&A, 682, A53
Planck Collaboration, Aghanim, N., Ashdown, M., et al. 2016, A&A, 596, A109
Rémy-Ruyer, A., Madden, S. C., Galliano, F., et al. 2014, A&A, 563, A31
Rhoads, J. E., Wold, I. G. B., Harish, S., et al. 2023, ApJL, 942, L14
Richardson, C. T., Simpson, C., Polimera, M. S., et al. 2022, ApJ, 927, 165
Richardson, C. T., Wels, J., Garofali, K., et al. 2025, arXiv:2505.07749
Rickards Vaught, R. J., Hunt, L. K., Aloisi, A., et al. 2025, ApJ, 990, 111
Rickards Vaught, R. J., Sandstrom, K. M., & Hunt, L. K. 2021, ApJL, 911, L17
Rigby, J., Perrin, M., McElwain, M., et al. 2023, PASP, 135, 048001
Rodríguez, M. J., Lee, J. C., Indebetouw, R., et al. 2025, ApJ, 983, 137
Satyapal, S., Vega, D., Dudik, R. P., Abel, N. P., & Heckman, T. 2008, ApJ, 677, 926
Schaerer, D., Contini, T., & Pindao, M. 1999, A&AS, 136, 35
Schaerer, D., Fragos, T., & Izotov, Y. I. 2019, A&A, 622, L10
Schaerer, D., & Stasińska, G. 1999, A&A, 345, L17
Schaerer, D., & Vacca, W. D. 1998, ApJ, 497, 618
Schlafly, E. F., & Finkbeiner, D. P. 2011, ApJ, 737, 103
Schlegel, D. J., Finkbeiner, D. P., & Davis, M. 1998, ApJ, 500, 525
Sharma, S., Corbelli, E., Giovanardi, C., Hunt, L. K., & Palla, F. 2011, A&A, 534, A96
Shenar, T., Hainich, R., Todt, H., et al. 2016, A&A, 591, A22
Smith, L. J., Bajaj, V., Ryon, J., & Sabbi, E. 2020, ApJ, 896, 84
Soria, R., Pakull, M. W., Motch, C., et al. 2021, MNRAS, 501, 1644
Speagle, J. S., Steinhardt, C. L., Capak, P. L., & Silverman, J. D. 2014, ApJS, 214, 15
Stanway, E. R., Eldridge, J. J., & Becker, G. D. 2016, MNRAS, 456, 485
Stefanon, M., Bouwens, R. J., Labbé, I., et al. 2021, ApJ, 922, 29
Sturm, E., Lutz, D., Verma, A., et al. 2002, A&A, 393, 821
Sun, J., He, H., Batschkun, K., et al. 2024, ApJ, 967, 133
Sutherland, R., Dopita, M., Binette, L., & Groves, B., 2018 MAPPINGS V: Astrophysical Plasma Modeling Code, Astrophysics Source Code Library, ascl:1807.005
Sutherland, R. S., & Dopita, M. A. 2017, ApJS, 229, 34
Tarantino, E., Bolatto, A. D., Indebetouw, R., et al. 2024, ApJ, 969, 101
Thornley, M. D., Förster Schreiber, N. M., Lutz, D., et al. 2000, ApJ, 539, 641
Thuan, T. X., Bauer, F. E., Papaderos, P., & Izotov, Y. I. 2004, ApJ, 606, 213
Thuan, T. X., & Izotov, Y. I. 2005, ApJS, 161, 240
Trump, J. R., Arrabal Haro, P., Simons, R. C., et al. 2023, ApJ, 945, 35
van Dishoeck, E. F., & Black, J. H. 1988, ApJ, 334, 771
van Dokkum, P. G. 2001, PASP, 113, 1420
van Hoof, P. A. M. 2018, Galax, 6, 63
van Zee, L., Westpfahl, D., Haynes, M. P., & Salzer, J. J. 1998, AJ, 115, 1000
Verma, A., Lutz, D., Sturm, E., et al. 2003, A&A, 403, 829
Vilchez, J. M., & Pagel, B. E. J. 1988, MNRAS, 231, 257
Virtanen, P., Gommers, R., Oliphant, T. E., et al. 2020, NatMe, 17, 261
Weedman, D. W., Hao, L., Higdon, S. J. U., et al. 2005, ApJ, 633, 706
Weingartner, J. C., & Draine, B. T. 2001, ApJ, 548, 296
Whitaker, K. E., Franx, M., Leja, J., et al. 2014, ApJ, 795, 104
White, S. D. M., & Frenk, C. S. 1991, ApJ, 379, 52
Whitmore, B. C., Chandar, R., Lee, J. C., et al. 2025, ApJ, 982, 50
Wise, J. H., & Cen, R. 2009, ApJ, 693, 984
Wu, Y., Charmandaris, V., Hunt, L. K., et al. 2007, ApJ, 662, 952
Yoshimoto, M., Yoneyama, T., Noda, H., Odaka, H., & Matsumoto, H. 2024, ApJ, 970, 8
Zhou, L., Shi, Y., Zhang, Z.-Y., & Wang, J. 2021, A&A, 653, L10